

Sentinel-1 SAR-based Globally Distributed Landslide Detection by Deep Neural Networks

Lorenzo Nava^a, Alessandro Mondini^b, Kushanav Bhuyan^a, Chengyong Fang^c, Oriol Monserrat^d, Alessandro Novellino^e and Filippo Catani^a

^a Machine Intelligence and Slope Stability Laboratory, Department of Geosciences, University of Padova, Padova, Italy;

^b National Research Council, Research Institute for Applied Mathematics and Information Technologies, Genova, Italy;

^c State Key Laboratory of Geohazard Prevention and Geoenvironment Protection, University of Technology, Chengdu, China;

^d Department of Remote Sensing, Geomatics Research Unit, Centre Tecnologic de Telecomunicacions de Catalunya (CTTC), Barcelona, Spain;

^e British Geological Survey, Nicker Hill, Keyworth, Nottingham, UK;

This manuscript is a preprint and will be shortly submitted for publication to a scientific journal. As a function of the peer-reviewing process that this manuscript will undergo, its structure and content may change. If accepted, the final version of this manuscript will be available via the ‘Peer-reviewed Publication DOI’ link on the right-hand side of this webpage. Please feel free to contact any of the authors; we welcome feedback.

Corresponding author: Lorenzo Nava, lorenzo.nava@phd.unipd.it

Abstract: Efficient response to large and widespread multiple landslide events (MLEs) demands rapid and effective landslide detection. Despite extensive efforts using optical remotely sensed imagery, limitations in global, day & night, and all-weather operational capabilities remain. To address these gaps, we introduce an approach that harnesses Deep Neural Networks (DNNs) and Synthetic Aperture Radar (SAR) backscatter data. This approach is designed through the analysis of 11 earthquake-induced MLEs, encompassing approximately 73 thousand landslides that occurred worldwide in a variety of different geo-settings. We test the reproducibility of the model results on unseen earthquake-induced landslides that occurred in Sumatra and Haiti. The top-performing model achieved a test F1-score of 82% in rapid assessment, indicating significant progress compared to previous attempts. The approach harnesses the cloud computing resources of Google Earth Engine for Sentinel-1 SAR image acquisition and processing, complemented by local computing resources to utilize advanced image classification DNNs capabilities. Through explainable artificial intelligence, our study underscores the efficacy of change detection bands in their superior discriminative capacity to delineate landslide features, surpassing the utilization of backscatter data alone. Moreover, we observe an improved ability to detect landslides within multi-temporal information stacks as opposed to single post-event SAR images. Finally, we introduce the SAR-LRA Tool in its Beta version, providing a valuable resource for rapid and comprehensive all-weather global landslide assessment. The systematic use of the Tool promises to facilitate the timely response to future MLEs. Our work establishes a robust foundation for future research endeavors, wherein SAR and DNNs can be harnessed to identify natural hazards and/or specific earth surface changes in mountainous regions. Given the frequent and increasing occurrence of MLEs, the development of a robust modeling approach is imperative to timely assess the spatial distribution of these phenomena. This research will pave the way for efficient rapid assessment of MLEs in the future.

Keywords: Landslides; SAR; Deep Learning; Remote Sensing; Earthquakes

Highlights

- Deep neural networks (DNNs) and Synthetic Aperture Radar (SAR) backscatter to globally detect landslides.
- Evaluate the impact of SAR temporal stack dimensions on DNN models.
- Calibrate generalized DNN models to rapid assess location landslides after major events in any weather and illumination conditions.
- Explainable artificial intelligence reveals landslide footprint in SAR.
- Introduce the SAR-based Landslide Rapid Assessment (SAR-LRA) Tool.

1. Introduction

Slope instabilities, commonly referred to as landslides, represent a widespread natural occurrence in mountainous and hilly regions, presenting substantial threats to both human lives and infrastructure (Froude and Petley, 2018). Earthquakes, heavy rainfall, and human activities serve as the primary triggers for landslides (Ferrario, 2019; Serey et al., 2019; Song et al., 2019; Wang et al., 2019). Notably, a single event can involve either one or multiple landslide failures (Guzzetti et al., 2012), commonly referred to as multiple landslide events (MLEs). Over the last 15 years, several MLEs have occurred, impacting wide regions within remarkably brief timeframes. Notable earthquake events include the devastating Wenchuan earthquake in China (2008), the Kaikōura earthquake in New Zealand (2016), and the Jiuzhaigou earthquake in China (2017). Additionally, earthquakes in Porgera, Papua New Guinea (2018); Hokkaido, Japan (2018); Lombok, Indonesia (2018); Haiti (2021); Sumatra, Indonesia (2022); and Turkey (2023) have all had profound impacts on their respective regions. Rainfall-triggered landslides also have triggered MLEs, such as the occurrences in Kedarnath, India (2013), Dominica (2017), Rolante, Brazil (2017), Belluno, Italy (2018), Hpa-An, Myanmar (2018), Uvira, Democratic Republic of the Congo (2020), and Malawi (2023). In the aftermath of such occurrences, it is important to investigate locations of landslides to assess damages to both natural and anthropogenic landscapes. Both Williams et al. (2018) and Amatya et al. (2023) highlighted the importance of rapid mapping for the 2015 Gorkha and 2021 Haiti MLE coseismic landslides, emphasizing the use of Synthetic Aperture Radar (SAR) data, preferably in an automated pipeline for emergency evacuations.

Moreover, a comprehensive understanding of these slope instability processes begins with a spatial assessment of the slope failures for both rainfall (Nocentini et al., 2023; Segoni et al., 2014) and earthquake-induced landslides (Meena and Tavakkoli Piralilou, 2019). Data concerning the location and timing of failed slopes is usually recorded in products also known as landslide inventories (Van Den Eeckhaut et al., 2013). These inventories also contain crucial information, about the typology (Rana et al., 2022, 2021), and details on the volume of the failure, offering a comprehensive overview of the characteristics and magnitude of the slope failure (Bhuyan et al., 2024; Parker et al., 2011).

Traditionally, the accurate positioning for landslides involved mainly the Global Satellite Navigation System (GNSS), topographic total station, and aerial photogrammetry surveys, known for their accuracy. However, these surveys are expensive, pose risks in challenging terrains (Manconi et al., 2014), and are exceptionally time-consuming, particularly during rapid assessments of MLE affecting large areas where time is of the essence (Williams et al., 2018). As a result, satellite products have emerged as a cost-effective alternative for generating landslide inventories (Ghorbanzadeh et al., 2019). The field of remote sensing, particularly Earth observation (EO) imagery analysis, has been extensively investigated for extracting landslide location. However, a significant portion of global slope failure lacks comprehensive and timely information (Guzzetti et al., 2012). This deficiency stems from the limitations and lack of systematic coverage in existing EO data (Williams et al., 2018). The challenge is exacerbated by the reliance on traditional and innovative methods for landslide detection on optical imagery. This approach is generally precise, however, limited when solar reflection is absent, or in presence of cloud obscuration. Numerous research has recently combined optical and multispectral data with deep learning (DL) models for landslide detection (Novellino et al., 2024). These approaches range from utilizing crowdsourced data (Catani, 2021) and Unmanned Aerial Vehicles (UAVs) (Beni et al., 2023; Dai et al., 2023a) to analyzing LIDAR (Fang et al., 2022), and satellite imagery (Bhuyan et al., 2023; Prakash et al., 2021). Some studies have also investigated the incorporation of morphological factors alongside satellite data for DL-based landslide detection (Meena et al., 2021). Moreover, there is a growing trend towards training DL models capable of delivering reliable predictions in unseen areas for swift assessment of new MLEs. We find studies focusing on a single data source, such as Copernicus Sentinel-2 (Prakash et al., 2021), and PlanetScope (Meena et al., 2023), while others explore the integration of multisource data (Xu et al., 2024) to enhance accuracy and improve transferability.

However, persistent clouds hinder the timely acquisition of data, impeding effective disaster management operations (Mondini et al., 2021a). This issue is prevalent in numerous tropical countries and is universally present in the context of landslide activations induced by storms (Wilson and Jetz, 2016) or where, following earthquakes that triggered MLEs, the first cloud-free optical image is not rapidly available (Williams et al., 2018).

SAR sensors represent a valuable alternative due to their capacity to acquire information on the ground in all-weather and illumination conditions (Hertel et al., 2023). While the phase information contained in the SAR images has been extensively employed in multi-temporal differential interferometric approaches (also known as InSAR) for monitoring slow-moving landslides (Antonello et al., 2004; He et al., 2023), InSAR is less effective in detecting rapid motions (He et al., 2023) and, therefore, recently, there has been a growing interest in using the amplitude information to identify and rapid landslide failures ((Burrows et al., 2020, 2019; Catani et al., 2005; Chorowicz et al., 1998; Mondini et al., 2019; Santangelo et al., 2022; Singhroy, 1995). Recent advancements include quantitative methods (Esposito et al., 2020; Jung and Yun, 2020). Landslides are identified as anomalies in SAR products based on tone, texture, pattern, mottling, or their changes (Santangelo et al., 2022). Singhroy (1995) introduced visual interpretation using C-HH airborne SAR to enhance landslide inventories in the Fraser River Valley, Canada. Mondini et al. (2019) systematically analyzed spaceborne C-band Sentinel-1 SAR images for landslide detection. Lindsay et al. (2023) propose a conceptual model for interpreting landslide expressions in SAR backscatter data. Research has explored mapping landslides by applying threshold values to changes in backscattering coefficients. (Konishi and Suga, 2018; Suga and Konishi, 2012) mapped landslides in Japan using X-band COSMO-SkyMed images. (Uemoto et al., 2019) used airborne Pi-SAR2 images to map landslides triggered by the 2016 Kumamoto earthquake. Handwerger et al. (2022) tested density heatmaps with Sentinel-1 C-band data over several MLEs. Mondini, (2017) conducted rainfall-induced landslide detection in Myanmar using C-band Sentinel-1 images. Ge et al. (2019) studied landslides triggered by the 2018 Hokkaido earthquake using L-band ALOS-2. (Aimaiti et al., 2019) utilized decision-tree-based modeling. However, while most of these methods have demonstrated the ability to successfully detect landslides in individual test areas, the issue of reproducibility in different settings and with different satellite data persists (Mondini et al., 2021b).

While artificial intelligence shows promise in training generalized models for automatically assessing target locations using satellite imagery, the focus on optical-based automated landslide detection outweighs studies utilizing SAR data, as noted by (Mondini et al., (2021b) Challenges like data pre-processing (Plank et al., 2016) and acquisition geometry distortions, particularly in high-slope landslide-prone regions, contribute to this disparity. Instances, where SAR and DL are combined for landslide detection, remain rare. Noteworthy, (Nava et al., 2022b, 2022a) demonstrated promising results by employing SAR Sentinel-1 amplitude data and DL convolutional neural networks (CNNs) in Hokkaido, Japan. Additionally, Shi et al., 2023) evaluated automated approaches in Papua New Guinea and Milin using maximum likelihood estimation (MLE). However, a comprehensive approach, specifically focusing on a globally distributed Sentinel-1 SAR-based landslide detection approach using deep learning, is currently missing.

In this study, we propose a generalized approach that combines Sentinel-1 SAR backscatter, and DNNs for rapid landslide detection in all-weather and day-night conditions. We develop this method by using 11 earthquake-induced MLEs, comprising a total of 73 thousand landslides. We test the approach on unseen MLEs, located in Sumatra and Haiti, to validate the generalizability and applicability of the approach. We use eXplainable AI (XAI) to examine the pixel contributions that influence the model's "decision-making" process. This approach unveils distinctive landslide signatures within SAR data. Finally, we propose the SAR-based Landslide Rapid Assessment tool (SAR-LRA) for rapid all-weather day-night assessment of MLEs. SAR-LRA can assess the location of landslides as soon as a single post-event image is acquired by the Sentinel-1 satellite and leverages the cloud-computing capabilities of Google Earth Engine (GEE), in conjunction with the user's local machine for the DNNs deployment. This research will lay the groundwork for a more efficient and rapid assessment of MLEs.

2. Earthquake-triggered MLE

For our analysis, we utilize 11 earthquake-triggered MLEs distributed geographically across the globe (see Figure 1), representing different environments and geological conditions.

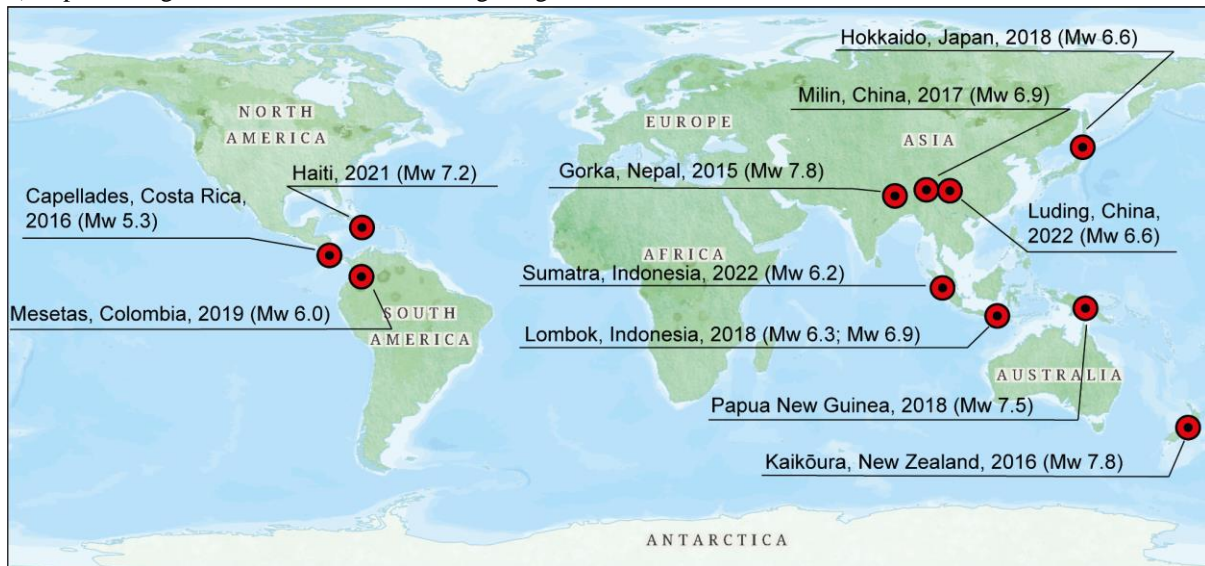


Figure 1: Location of the 11 earthquake-triggered MLEs investigated.

2.1 Gorka, Nepal, 2015 (Mw 7.8)

The Himalayan region, recognized for its seismic risk due to the India-Asia continental convergence at approximately 45 mm/year (Sella et al., 2002), has witnessed major earthquakes, including the notable Mw 7.8 Gorkha earthquake in 2015, causing nearly 9,000 deaths and significant economic damage. This area is also prone to high landslide risks, intensified by its steep terrain and heavy monsoon rains.

We use the landslide inventory from (Roback et al., 2017) which is openly provided in the USGS ScienceBase Catalog (<https://www.sciencebase.gov/catalog/>). The authors mapped the co-seismic landslides using high-resolution satellite imagery at pre- and post-event windows. Specifically, DigitalGlobe Worldview-2 and -3, and Pleiades imagery were used with resolutions ranging from 20-50 cm. The authors found landslides connected exclusively with the main shock on April 25, however in certain cases, the imagery was not available until after the 12 May Mw7.2 aftershock. They identified 24,915 landslides with a total area of 87 km².

2.2 Kaikōura, New Zealand, 2016 (Mw 7.8)

The 2016 Kaikōura earthquake, a seismic event of magnitude 7.8 that occurred on 14 November in the South Island of New Zealand, had its epicenter approximately 60 km southwest of Kaikōura. This significant earthquake set in motion over 10,000 landslides in sparsely populated areas, fortunately resulting in no reported landslide-related fatalities (Tanyaş et al., 2022a). Despite the absence of casualties, the landslides caused extensive damage to infrastructure and created blockages in rivers at multiple locations.

We use the open-source landslide inventory digitized by Tanyaş et al. (2022), and freely available in the supplementary materials of their publication. A comprehensive analysis of landslides was conducted utilizing sets of optical Sentinel-2 satellite images with a 10 m resolution for both pre- and post-earthquake conditions. Specifically, nine pre-seismic images, acquired between September 13 and October 26, 2016, and nine post-seismic images, acquired between November 22 and December 15, 2016, were employed. In total, 14,233 individual landslides were meticulously mapped, covering an extensive area of approximately 14,000 square km. The authors also validate whether the mapped landslides were triggered by the earthquake rather than subsequent rainfall events, high-resolution images from Google Earth were utilized.

2.3 Capellades, Costa Rica, 2016 (Mw 5.3)

Coseismic landslides are a major concern in Costa Rica, causing over \$100 million US in damages since 2009 and being the leading cause of fatalities during recent earthquakes. The country has a recorded history of at least 23 earthquakes with a magnitude greater than 5.5 since 1772, which have led to various types of landslides (Ruiz

et al., 2020). The district of Capellades in Costa Rica was one of the regions that was heavily affected by the seismic activity of the 2016 earthquake (Mw 5.3) that triggered multiple landslides. Historically, the country has been hit by landsliding due to earthquakes caused by subduction processes.

We use the open-source inventory of landslides from Ruiz et al. (2020). The inventory was curated via field surveys along with remote sensing techniques such as LIDAR, satellite imagery, drone photography, and a detailed Digital Elevation Model (DEM; showing 20 m elevation contours) of Costa Rica to map landslide distributions.

2.4 Milin, China, 2017 (Mw 6.9)

The area investigated encompasses the region affected by the Milin earthquake. The Milin earthquake, occurring on November 18, 2017, registered a magnitude of Mw 6.9, marking it as the third-largest seismic event in the region since 1950. Its epicenter lies within the active Bomi-Medog structural belt, specifically on the NW-SE Xixingla fault, surrounded by other active thrust faults such as the Nujiang, Jiali, Aparon, NE-NNE Milin, Medog, and Yarlung Tsangpo faults (Hu et al., 2019). The earthquake affected six counties, including Milin, Bayi, Medog, Chayu, Bomi, and Gongbo'gyamda, impacting over 12,000 individuals and causing damage to various infrastructures, including around 3000 houses, roads, communication lines, flood prevention embankments, and irrigation canals.

We use the open-source inventory digitized by Hu et al. (2019) freely available in the supplementary materials and in the USGS ScienceBase Catalogue (<https://www.sciencebase.gov/catalog/>). Their analysis included post-earthquake satellite images from Spot 7, featuring a resolution of 1.3 meters, and Sentinel, with a resolution of 9.4 meters. Additionally, pre-earthquake satellite images from Landsat 7 ETM, with a resolution of 15 meters, and Google Earth were used. A total of 939 landslides were identified, encompassing an area of 37.65 square kilometers. Among these, 766 landslides, covering an area of 33.61 square kilometers, were attributed to the Milin earthquake. This inventory was digitized by comparing satellite images taken before and after the seismic event (specifically, Landsat 7 ETM on November 5, 2017, and Spot 7 on December 12, 2017).

2.5 Papua New Guinea, 2018 (Mw 7.5)

Papua New Guinea (PNG), situated on the Australian continent, constitutes the eastern portion of New Guinea. This area, marked by active volcanoes, earthquakes, and steep elevations reaching up to 4400 meters above sea level, is situated within the Pacific Ocean's "Ring of Fire." On February 25, 2018, a powerful earthquake with a magnitude of Mw 7.5 struck the southern region of the Papuan Fold and Thrust belt, particularly affecting the central highlands of PNG. This earthquake, the most significant in the region in the past century, caused substantial damage to buildings and energy structures, triggering a large number of landslides. Characteristics of the landslides included high relief, steep slopes, and weak lithology (Tanyaş et al., 2022b).

We use the open-source inventory digitized by Tanyas et al. (2022), and freely available in the supplementary materials and in the USGS ScienceBase Catalogue (<https://www.sciencebase.gov/catalog/>). In their comprehensive mapping effort, the authors identified a total of 11,607 landslides covering an expansive area of 185 square km. Notably, large landslides are prevalent throughout the study area, with over half of the mapped landslides exhibiting a planimetric area exceeding 50,000 square m. Further analysis by the authors reveals that the mainshock directly triggered 10,469 landslides. In contrast, the remaining 1138 landslides were induced by either aftershocks or subsequent rainfall events occurring between February 26 and March 19.

2.6 Lombok, Indonesia, 2018 (Mw 6.3 and Mw 6.9)

The study area encompasses the northern part of Lombok Island, covering 1798 km². This region is particularly prone to landslides due to its rugged terrain, dominated by the Rinjani Volcanic Complex, which includes Mt. Rinjani at 3726 meters above sea level and the Samaras caldera, now occupied by Lake Segara Anaka. Between July and August 2018, Lombok experienced a series of four earthquakes exceeding magnitude 6.0, beginning with a 6.4 event on July 28, followed by a stronger 6.9 quake on August 5, and two subsequent events on August 19 (Mw 6.3 and Mw 6.9) (Ferrario, 2019).

We use the open-source inventories digitized by Ferrario (2019), and freely available in the supplementary materials and in the USGS ScienceBase Catalogue (<https://www.sciencebase.gov/catalog/>). Landslides were mapped through visual interpretation of high-resolution aerial images, utilizing Sentinel-2 data for an overview

and PlanetScope imagery for detailed mapping. Ortho-rectified multispectral tiles were used. Landslide identification relied on the contrast in color and texture between pre- and post-event imagery. The inventory focused on the aftermath of the Mw 6.4 event on July 28, 2018, and the Mw 6.9 event on August 5, 2018. Pre-existing landslides observed in July 2018 images were included if reactivated. For this research, we merge the inventories, considering them appertaining to the same event. This is to avoid including landslides in the pre- or post-event temporal stacks. In this case, the pre-event stack ends on July 28, 2018, while the post-event stack starts on August 5, 2018.

2.7 Hokkaido, Japan, 2018 (Mw 6.6)

The 2018 Iburi earthquake occurred on September 5th in Hokkaido, encompassing the eastern and central Iburi regions of Northern Japan. Striking just one day following the passage of Typhoon Jebi, the mainshock (Mw 6.6) centered in Atsuma, approximately 300 km southeast of the Kuril Trench. Registering a maximum seismic intensity of 7.0 on the JMA scale (equivalent to approximately X on the MMI scale), the earthquake inflicted significant devastation, resulting in 41 fatalities, 691 injuries, and extensive damage to hundreds of residences (Wang et al., 2019). Despite a subsequent decrease in seismic activity, a succession of persistent aftershocks ensued, with JMA recording 311 aftershocks surpassing a seismic intensity of 1.0 by October 31st, 2018.

We use the open-source inventories digitized by Wang et al. (2019) and freely available in the Data Availability section of their paper. The authors digitize a total of 7837 landslides from PlanetScope satellite images. To ensure the thoroughness of the assessment, neighboring zones were analyzed using large swath images obtained from Landsat 8 OLI and Sentinel-2 satellites after the earthquake. No additional slope failures were identified for the study area related to this seismic event. Analysis of satellite images, aerial images, and video footage from news broadcasts suggests that the coseismic landslides associated with the 2018 Hokkaido earthquake are predominantly characterized as small-scale shallow debris slides.

2.8 Mesetas, Colombia, 2019 (Mw 6.0)

The study area is situated on the eastern foothills of the Colombian Eastern Cordillera. The Mesetas Earthquake, with a magnitude of $M_w = 6.0$, occurred in the eastern foothills of the Eastern Cordillera of Colombia on December 24, 2019, as reported by (Poveda et al., 2022). The quake struck at a depth of approximately 13 ± 2.9 km. Shortly after the main event, an aftershock measuring Mw 5.8 occurred (Poveda et al., 2022)

We use the open-source rapid response inventory digitized by Garcia-Delgado et al. (2019), and freely available in the supplementary materials and in the USGS ScienceBase Catalogue (<https://www.sciencebase.gov/catalog/>). The inventory was meticulously constructed following specific criteria outlined by (Tanyaş et al., 2017) to ensure its reliability: full coverage of the affected area; inclusion of all triggered landslides regardless of their size; representation of each landslide as a polygon rather than a point; efforts to distinguish landslides triggered before and after the earthquake; classification of landslides, at least by type; and validation of the inventory through field observations. The authors used pre- and post-earthquake multi-spectral satellite imagery from sources like Sentinel 2 and PlanetScope, along with medium-resolution Digital Elevation Models (DEM).

2.9 Haiti, 2021 (Mw 7.2)

The M 7.2 Nippes, Haiti, earthquake struck at 12:29:08 UTC on August 14, 2021, with its epicenter located in the Tiburon Peninsula, 125 km west of Port-au-Prince. The rupture primarily moved westward along the Enriquillo-Plantain Garden fault zone, terminating near Pic Macaya National Park. Severe shaking, exceeding 0.5 g, affected an 80-km band of steep and rugged terrain, heightening landslide susceptibility (Martinez et al., 2021). USGS near-real-time ground failure assessments estimated significant landslide occurrence, covering approximately 70 square kilometers, endangering around 9,000 individuals. Tropical Cyclone Grace, following the earthquake, likely exacerbated landslide risks by depositing 5–10 inches of rain in Haiti on August 16, 2021.

We use the open-source rapid response inventory digitized by Martinez et al. (2021), and freely available in the supplementary materials and in the USGS ScienceBase Catalogue (<https://www.sciencebase.gov/catalog/>). Martinez et al. (2021) conducted a preliminary inventory of landslides using mid- to high-resolution satellite imagery and a high-resolution DEM. Their analysis utilized imagery from Sentinel-2, WorldView, and Planet satellites, along with lidar-derived DEM data. The authors compared pre- and post-earthquake images to confirm co-seismic landslide. Due to image quality variations and rapid response mapping, they estimate their accuracy

within tens of meters, with a maximum error of 45 meters for certain images. The inventory documents 4,893 landslides, though this is likely a conservative count due to limited imagery availability and cloud cover.

2.10 Luding, China, 2022 (Mw 6.6)

The Luding earthquake of 2022 (Mw 6.6) took place along the Hengduan Mountains at the southeastern edge of the Qinghai-Tibet Plateau, characterized by its steep alpine canyon geography. The area's subsurface is primarily composed of acid-plutonic rocks and various sedimentary rocks (Dai et al., 2023b). This earthquake's epicenter was near the Moxi Fault, located in the southeastern stretch of the Xianshuihe Fault, which runs northwest to southeast.

We used the inventory data from Dai et al. (2023b), where the landslides were mapped using manual interpretation of high-resolution composite images via multi-temporal images. These images were acquired from PlanetScope, Gaofen-2, Gaofen-6, and UAV drone surveys. Around 5336 landslides were recorded, covering a total of 28.53 km² of coseismic landslides. Significant landslide activity has been observed on both sides of the Xianshuihe Fault within Detuo and Tianwan towns, with the size of individual landslides in these areas being among the largest seen in the earthquake zone.

2.11 Sumatra, Indonesia, 2022 (Mw 6.1)

On February 25, 2022, a magnitude 6.1 earthquake rocked West Sumatra, Indonesia, occurring at a shallow depth of only 4.9 km. The earthquake's epicenter was approximately 20 km away from Mount Talakmau, a compound volcano with an elevation of around 3,000 m. Mount Talakmau is believed to have been active during the Holocene period. Geologically, the volcano is composed of andesite and basalt rocks dating back to the Pleistocene-Holocene age (Basofi et al., 2016). The region experiences a humid tropical climate, with mean annual precipitation ranging between 3500 and 4500 mm per year in the West Pasaman area. The Mw 6.1 earthquake struck West Sumatra on February 25, 2022, triggering numerous landslides across a 6 km² area along the eastern and northeastern flanks of Mount Talamau.

The landslides were manually digitized using pre- and post-event PlanetScope imagery, consistent with the methodology outlined in (Meena et al., 2023).

3. Data

3.1 Sentinel-1 SAR data from Google Earth Engine

The Sentinel-1 constellation offers improved revisit capabilities compared to earlier SAR missions such as ERS-1/2 and Envisat ASAR. While maintaining broad area coverage, it surpasses its predecessors by providing higher resolution and the potential for global dual-polarization coverage over landmasses. Each Sentinel-1 satellite follows a near-polar, sun-synchronous orbit with a 12-day repeat cycle, completing 175 orbits per cycle. Sentinel-1A and Sentinel-1B are positioned in the same orbital plane but with a 180° orbital phase difference. With a single satellite, global landmass mapping in Interferometric Wide swath mode occurs approximately every 12 days, while the two-satellite constellation enables a more frequent 6-day exact repeat cycle at the equator. Notably, Sentinel-1B has been inactive since 2022, and it is in the process of being substituted by an equivalent platform. Revisit rates vary with latitude, with higher revisit frequencies observed at higher latitudes compared to the equator (<https://sentinels.copernicus.eu/web/sentinel/user-guides/sentinel-1-sar/revisit-and-coverage>). We used GRD scenes 10 meters spatial resolution, and Interferometric Wide (IW) acquisition mode. Depending upon the availability, each scene consists of either one or two out of four possible polarization bands, determined by the instrument's polarization settings. The potential combinations include single-band Vertical Vertical (VV) polarization or Vertical Horizontal (VH) polarization, and dual-band VV+VH, each representing different co-polarization or cross-polarization scenarios. Additionally, each scene incorporates an 'angle' band indicating the approximate incidence angle from the ellipsoid in degrees at each point. Pre-processing of each scene involves the following steps using the Sentinel-1 Toolbox (<https://sentinel.esa.int/web/sentinel/toolboxes/sentinel-1>): Thermal noise removal, Radiometric calibration, and Terrain correction utilizing SRTM 30 or ASTER DEM for latitudes exceeding 60 degrees, where SRTM data is unavailable. The final terrain-corrected values are logarithmically scaled ($10 \cdot \log_{10}(x)$ dB) (https://developers.google.com/earth-engine/datasets/catalog/COPERNICUS_S1_GRD). For a comprehensive understanding of the pre-processing steps, refer to <https://developers.google.com/earth-engine/guides/sentinel1>. Our research focuses on scenarios

where either only VV polarization or both VV and VH polarizations are accessible for both ascending and descending orbits (see Table 1).

Table 1: Sentinel-1 polarizations and orbits accessible for each study case which respect the requirements of the designed study. Lastly, the number of landslides in the used inventories is shown for each MLE.

Study Case	Polarizations	Orbits	Date of the event	Number of landslides
Gorka	VV	Ascending; Descending	25 April 2015	24,903
Kaikoura	VV	Ascending; Descending	14 November 2016	14,168
Capellades	VV	Ascending; Descending	01 December 2016	51
Milin	VV, VH	Ascending; Descending	18 November 2017	766
Papua New Guinea	VV, VH	Ascending; Descending	26 February 2018	4,584
Lombok	VV, VH	Ascending; Descending	5 August 2018; 19 August 2018	12,688 (total)
Hokkaido	VV, VH	Ascending; Descending	6 September 2018	5,625
Mesetas	VV, VH	Ascending; Descending	5 August 2019	837
Haiti	VV, VH	Ascending; Descending	14 August 2021	4,887
Luding	VV, VH	Ascending; Descending	5 September 2022	5,006
Sumatra	VV, VH	Ascending, Descending	25 February 2022	171

4. Methods

The SAR imagery undergoes a series of pre-processing steps using cloud computing on GEE. For each study area, we acquire and stack the necessary images in space and time, extract the median values, and generate shadowing and layover masks. Subsequently, we calculate the change detection bands and composite the final images. Once the processing is complete, the images are downloaded to the local machine for further analysis. The subsequent data processing involves creating datasets, as outlined in Section 4.1, to prepare the data for model training. This involves organizing the downloaded imagery and associated metadata into structured datasets suitable for input into the model training pipeline. During the landslide detection phase, we adhere to the same processing pipeline to maintain consistency with the training data. The downloaded images undergo the same processing steps, ensuring uniformity in the data preprocessing procedure. Once the images are prepared, we apply the object detection procedure outlined in Section 4.3.3.

4.1 Dataset creation

Four distinct combinations of Sentinel-1 SAR polarizations and orbits have been devised to evaluate neural network classification performance. These combinations include (i) solely VV polarization, and (ii) both VV and VH polarizations, in two orbits—ascending and descending (see Table 2). We also calculate the differences for

both pre-and post-VV and VH amplitude imagery, represented as $diffVV$ and $diffVH$, respectively. These values are derived by subtracting the median amplitude of the pre-event stack from the median amplitude of the post-event stack. Each polarization combination is separately employed with different orbits, enabling the independent assessment of the neural network's classification performance. This approach facilitates a comprehensive evaluation of the network's effectiveness.

Table 2: Main dataset combinations. $diffVV$ and $diffVH$ are obtained by subtracting the median of the pre-event stack from the median of the post-event stack.

Name	Orbit	Var 1	Var 2	Var 3	Var 4
VV	Ascending	VV post-event	$diffVV$	/	/
	Descending				
VV_VH	Ascending	VV post-event	VH post-event	$diffVV$	$diffVH$
	Descending				

Furthermore, these four major combinations are implemented across various pre- and post-event temporal buffers. Following this, the median is computed for each polarization within each stack. The selection of these buffers is based on the current average revisiting time of Sentinel-1. The 12-day buffer represents the most rapid assessment time, encompassing one acquisition per acquisition geometry, which will fall within 12 days of the event (ESA - Sentinel Online). We vary the selection of pre-event buffers to assess their impact on prediction accuracy in rapid assessment. Additionally, we expand the post-event buffer to observe its effect on prediction enhancement. We further assess the model's performance by pairing pre- and post-event temporal buffers (see Table 3). This approach provides a nuanced evaluation, considering the impact of specific buffer sizes on the model's classification performance.

Table 3: Temporal buffers to be applied to the combinations of Table 2.

Buffer pre-event (days)	365	240	120	60	60	60	12	24	48	60
Buffer post-event (days)	12	12	12	12	24	48	12	24	48	60

It is crucial to acknowledge that when working with two multitemporal stacks located in different geographic areas, even if they are generated using the same temporal buffers, they might not have the same number of images. This discrepancy can be attributed to differences in the orbit plans of Sentinel-1. A total of 28 datasets have been generated, encompassing all the above-mentioned combinations.

4.2.1 Data sampling

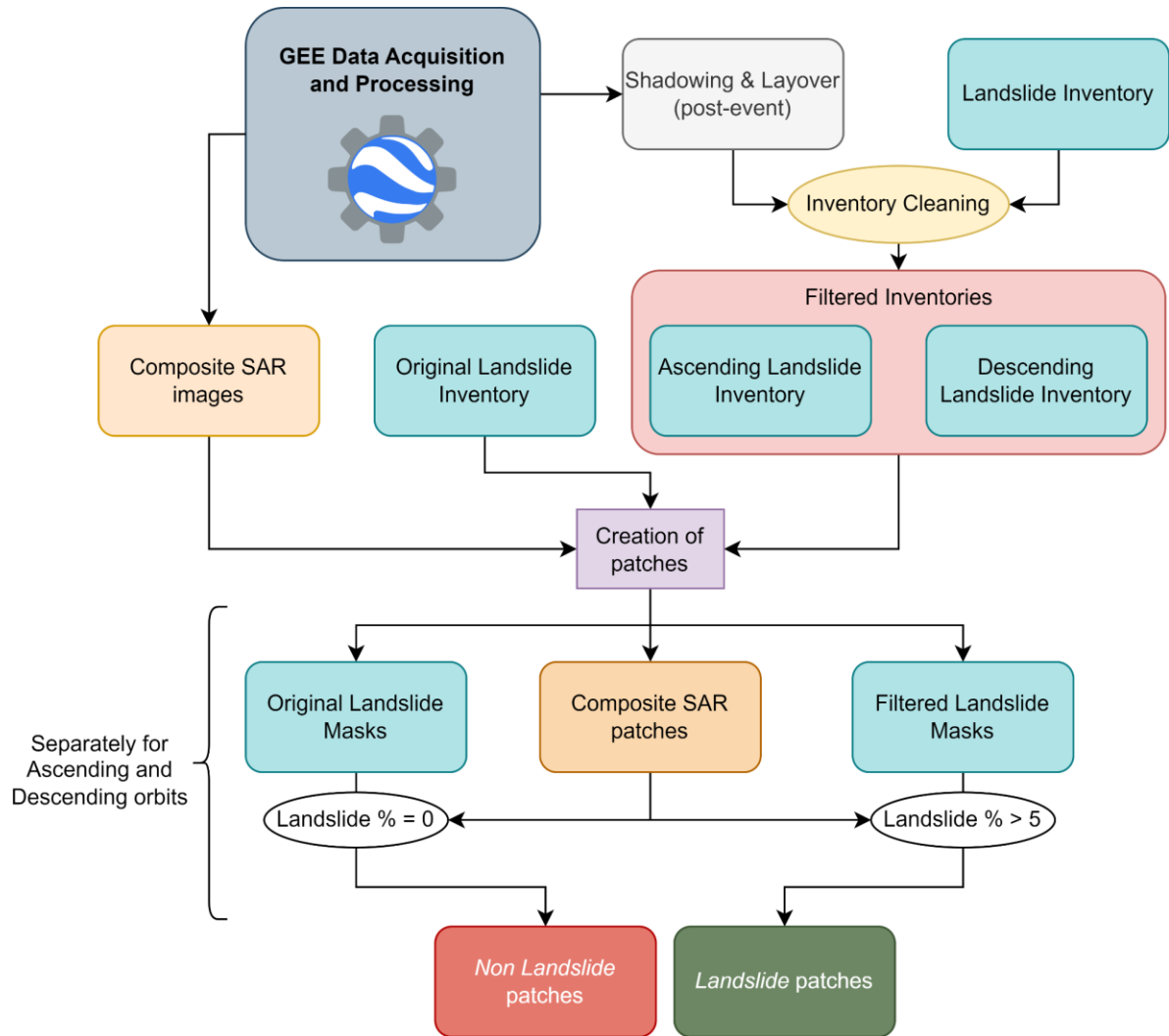


Figure 2: Workflow devised for generating the landslide dataset utilizing SAR data. This approach is iteratively applied for each dataset combination and temporal buffer assessed in our study (see Tables 2 and 3).

We extracted a rectangular Region of Interest (ROI) that closely aligns with the inventory boundaries. By visually interpreting Google Earth imagery, we ensure the completeness of the inventory within the specified area. Within the confines of the ROI, our approach incorporates a grid-based patch sampling methodology, designed to avoid any overlap between patches. We have chosen not to partition datasets geographically to avoid introducing biases into the model evaluation process. Consequently, removing the overlap aims to prevent including the same landslides in both the training and test sets during random splitting. The absence of overlap in our patch sampling methodology reinforces the reliability of our evaluation, promoting a more accurate and unbiased assessment of the model's performance. The variability in landslide dimensions across different cases precludes us from selecting a patch size solely based on their sizes. Generally, larger patches provide richer contextual information. However, excessively large patches yield final bounding boxes that are undesirably large. In our study, we settled on a patch size of 64x64 pixels, aiming for a final bounding box of approximately 0.4 square kilometers.

Given the intrinsic differences between SAR and optical data, it becomes crucial to exercise additional precautions throughout the data sampling process. A noteworthy distinction arises from the fact that the landslide polygons from the available inventories are traditionally designed using optical data. When using such inventories with SAR datasets, it is imperative to acknowledge and address the unique characteristics of SAR. The primary distinctions arise from the geometric distortions inherent in SAR (Del Soldato et al., 2021), particularly in hilly and mountainous terrains (Burrows et al., 2020). Shadowing and layover are particularly troublesome distortions because the affected pixels in these regions cannot convey information. Layover represents an extreme form of foreshortening, where the upper portions of a backscattering object, such as a mountain top, are recorded closer

to the radar (in slant range) than the lower parts, like the base of the slope. Shadows result from areas lacking radar illumination (Meyer, 2019). The extent of geometric distortions is influenced by satellite orbit parameters (e.g., ascending or descending), satellite configuration (e.g., side of look), and acquisition parameters (e.g., look angle, Θ) (Mondini et al., 2021b).

To address the potential bias introduced by including images labeled as *landslides* that lack relevant landslide-related information, we design an original sampling strategy reported as the “Inventory Cleaning” step in Figure 2. This involves calculating shadow and layover masks specific to the acquisition geometry and study case for each type of dataset outlined in Table 2. Then we subtract the masks from the landslide inventories. The methodology for extracting shadow and layover masks aligns with the approach proposed by Vollrath et al., (2020), as utilized by Lindsay et al., (2022). It's noteworthy that this extraction process is implemented without introducing spatial buffers, ensuring that the resulting masked area remains unaltered. This means that for each study case, three landslide inventories are used: (i) original inventory, (ii) inventory filtered with ascending shadowing and layover masks, and (iii) inventory filtered with descending distortion masks. The initial inventory serves as the basis for sampling the *background* class. Subsequently, the filtered inventories are utilized to sample the *landslide* class, with the requirement that the landslide images must comprise more than 5% of pixels classified as landslides. This threshold of 5% is chosen arbitrarily. Elevating this percentage could enhance model performance by enriching training and testing with more pronounced landslide signatures, potentially yielding higher scores. However, in deployment, the model may primarily detect cases with high landslide density due to the emphasis on stronger signatures. The 5% threshold corresponds to an area of approximately 2000 square meters.

An additional criterion is applied to the SAR images, whereby patches are discarded if they contain more than one pixel with a NaN (Not a Number) value. This condition is implemented to prevent the inclusion of incomplete SAR patches that may contain landslides within regions marked as NaN. By enforcing this condition, the dataset is safeguarded against potential issues arising from incomplete or corrupted SAR data, ensuring the robustness of the dataset for subsequent model training and evaluation.

Lastly, landslide detection is often a highly imbalanced binary classification problem (Nava et al., 2022a). Depending on the study case, the ratio of *background/landslide* in terms of the number of patches can range from approximately 8 (Hokkaido) to 120 (Gorka). Because of this, the evaluation of the performance of the models would heavily depend on the ratio, rather than on the SAR backscatter. Therefore, we opted to adjust the ratio of the test set to 10 in cases where the natural ratio was initially higher while maintaining it unchanged in instances where it was lower. Datasets with different ratios are instead created for the training sets to define the specific optimal imbalance.

4.3 Deep learning-based landslide classification

CNNs have demonstrated remarkable effectiveness in image classification tasks (e.g., Nava et al., 2022b; Tang et al., 2021; Zhang et al., 2017). Training a robust model heavily depends on having a large representative amount of training data (Shorten and Khoshgoftaar, 2019). For this study, we design a shallow, yet efficient CNN model for landslide detection. The model comprises an encoder and a classifier (see Figure A3). During the encoding phase, the input data shape is $H \times W \times C$ (Height x Width x Channels). Through three encoding modules, the data dimensions are transformed to $(H/4 \times W/4 \times 32)$. Each encoding module consists of a convolutional layer (Conv 3×3), normalization layer, and max-pooling layer. Subsequently, to fully consider global features and mitigate the impact of feature collapse resulting from dimensionality increase, we concatenate the multi-level features from the three encoding modules. After pooling and dropout operations, the concatenated features are fed into a Dense layer for classification using *sigmoid* activation. The architecture described is a modified version of the one utilized in (Nava et al., (2022b), which demonstrated promising results. We employed TensorFlow 2.8 (Abadi et al., 2016) for training the model, utilizing the Adam optimizer (Kingma and Ba, 2015) with a batch size of 500 and a focal loss function. The model underwent training for a maximum of 500 epochs, during which hyperparameter tuning was employed to optimize its performance. Additionally, early stopping was implemented to halt training when the validation loss ceased to decrease for consecutive 30 epochs. Utilized as the loss function in this study, the focal loss (Lin et al., 2017) represents a refined approach to addressing the inherent challenges of class imbalance and the effective handling of challenging examples within the context of binary classification tasks. Finally, the training of DL models necessitates the identification of optimal hyperparameter combinations

to maximize performance. As such, we conducted iterative training sessions employing various combinations of hyper-parameters and settings, specifically focusing on the number of filters (32, 64), class imbalance rate of the training set (ranging from 4 to 6), dropout rates (0.5, 0.7), and learning rates (10e-4, 10e-5). The evaluation of the model's performance involved the calculation of standard accuracy metrics, including Precision, Recall, and F1-score, which were derived from true positives (TP), true negatives (TN), false positives (FP), and false negatives (FN).

4.4 Landslide detection

The calibrated models are used in combination with a *sliding window* algorithm (Lee et al., 2001) and *non-maximum suppression* (Neubeck and Van Gool, 2006) to assess the locations of landslides inside a given area. The *sliding window* algorithm systematically extracts regions of interest (ROIs) across the study area, with a defined vertical and horizontal stride and dimension. In our approach, we set the vertical and horizontal stride of the *sliding window* algorithm to 32 pixels, ensuring a 50% overlap between adjacent ROIs. This overlap enhances the robustness of our analysis by capturing a diverse range of spatial features while maintaining computational efficiency. Additionally, we maintain the dimensions of the training patches at 64x64 pixels to ensure consistency with the characteristics of the training data. These ROIs, representing sub-images of the satellite imagery, are then classified using landslide classification models trained on labeled image data. The models classify each ROI as either a *landslide* or a *non-landslide*. Subsequently, *non-maximum suppression* is applied to refine the predictions by removing redundant or overlapping detections, ensuring that each *classified* landslide patch corresponds to a unique and significant area on the map. Despite being computationally more intensive than the classic YOLO (You Only Look Once) architecture (Han et al., 2023; Liu et al., 2023), we opt for this strategy due to the inherent characteristics of SAR data. Unlike optical imagery, SAR data may not consistently align landslide inventories with landslide information, leading to discrepancies in location. Additionally, landslide polygons often encompass multiple landslides or amalgamated features, making it impractical to mechanically design bounding boxes based on exact polygon extensions. This approach minimizes the risk of imprecision and oversized bounding boxes, ensuring more accurate delineation of landslide areas.

5. Results

We conduct a comparison of predictions using VV and VV_VH data in the six study cases to compare the models in the same areas. Additionally, we train the VV model on nine cases to enhance the generalizability of the model. Finally, we present the detection performance of the models in entirely new and unseen areas, as we were to detect landslides for a recently occurred unseen MLE.

5.1 Landslide classification results

In adherence to rigorous experimental standards, the test sets are meticulously curated to include a representative subset comprising 33% of patches from each distinct study case. These patches are carefully chosen to ensure that they remain entirely unseen by the models during training, thereby safeguarding the integrity of the evaluation process. Furthermore, to maintain data consistency, particular attention is given to the consistency of training and testing protocols across all experiments. Notably, for both VV and VV_VH combinations within the same stack, identical patches are employed for both model training and testing phases. This meticulous approach ensures a level playing field and facilitates a direct, unbiased comparison between the several data combinations.

The reported scores in Tables 4 and 5 represent the median values derived from an exploration across 24 distinct combinations of hyperparameters and training set class imbalances, as outlined in Section 4.4.2 (Model Training and Validation). This comprehensive analysis ensures robustness and reliability in the assessment of model performance across different stacks and orbit combinations. An overview of the most meaningful metric F1-score across the various data configurations is given in Figure 3. We notice that the precision trend remains relatively consistent across all combinations. However, the recall varies significantly, as does the F1 score. In numerous cases, both metrics experience a notable increase when incorporating additional post-event acquisitions.

Table 4: Median and standard deviation of the accuracy, precision, recall, and F1-score of the models trained on the various combinations of the VV_VH datasets. They are derived from the hyperparameters and training imbalance tuning computed comparing the predictions against the unseen composite test set.

Orbit	Stacks	Accuracy (%)	Precision (%)	Recall (%)	F1-score (%)
Ascending	365-12	95.48 ± 0.4	78.98 ± 4.0	77.16 ± 4.6	78.30 ± 2.3
	240-12	95.37 ± 0.4	81.13 ± 2.9	74.80 ± 4.8	77.30 ± 2.4
	120-12	95.62 ± 0.4	79.90 ± 3.0	78.23 ± 3.7	78.70 ± 2.3
	60-12	95.78 ± 0.2	82.32 ± 2.9	76.71 ± 2.3	79.45 ± 1.2
	12-12	95.31 ± 0.5	82.49 ± 5.1	72.60 ± 4.0	75.90 ± 1.9
	24-24	95.97 ± 0.4	83.61 ± 4.1	78.37 ± 3.0	80.10 ± 1.4
	60-24	96.23 ± 1.7	82.83 ± 6.8	80.05 ± 1.6	81.72 ± 1.4
	48-48	96.41 ± 2.0	82.55 ± 10.0	83.20 ± 11.6	83.03 ± 10.7
	60-48	96.29 ± 1.3	81.78 ± 6.7	83.74 ± 5.1	82.42 ± 5.5
	60-60	96.43 ± 1.5	81.27 ± 6.6	83.77 ± 1.2	83.24 ± 9.3
Descending	365-12	95.52 ± 0.4	79.79 ± 4.0	75.73 ± 3.4	77.54 ± 1.4
	240-12	95.41 ± 0.8	81.64 ± 6.0	73.46 ± 5.4	76.73 ± 3.4
	120-12	95.71 ± 0.4	82.01 ± 4.0	75.51 ± 2.0	78.73 ± 1.4
	60-12	95.52 ± 0.6	83.76 ± 5.3	72.53 ± 6.8	78.05 ± 3.5
	12-12	95.36 ± 0.3	83.90 ± 2.9	71.11 ± 3.9	76.30 ± 1.9
	24-24	95.97 ± 0.4	83.61 ± 4.1	78.37 ± 3.0	80.10 ± 1.4
	60-24	95.78 ± 0.4	79.53 ± 4.0	79.22 ± 2.8	79.71 ± 1.4
	48-48	96.41 ± 1.9	82.55 ± 10.2	83.20 ± 11.6	83.03 ± 10.8
	60-48	96.34 ± 0.4	81.66 ± 2.6	84.04 ± 2.5	82.8 ± 1.7
	60-60	96.47 ± 2.2	82.56 ± 11.2	83.87 ± 15.6	83.36 ± 13.6

Table 5: Median and standard deviation of the accuracy, precision, recall, and F1-score of the models trained on the various combinations of the VV datasets. They are derived from the hyperparameters and training imbalance tuning computed comparing the predictions against the unseen composite test set.

Orbit	Stacks	Accuracy (%)	Precision (%)	Recall (%)	F1-score (%)
Ascending	365-12	93.57 ± 1.4	71.26 ± 8.1	65.80 ± 4.6	67.85 ± 4.0
	240-12	93.55 ± 1.2	72.18 ± 8.6	63.50 ± 4.2	66.51 ± 3.2

	120-12	93.29 ± 1.3	69.88 ± 8.0	66.47 ± 5.0	67.33 ± 4.5
	60-12	91.59 ± 2.4	57.95 ± 17.2	65.74 ± 14.1	60.51 ± 13.7
	12-12	93.39 ± 0.8	74.68 ± 7.9	56.46 ± 3.8	64.03 ± 3.1
	24-24	94.41 ± 1.5	76.37 ± 9.1	71.68 ± 4.3	73.03 ± 4.2
	60-24	94.07 ± 1.2	71.35 ± 6.9	74.41 ± 5.2	71.89 ± 4.0
	48-48	95.31 ± 0.8	77.22 ± 5.4	78.18 ± 3.5	77.26 ± 2.7
	60-48	94.76 ± 1.7	74.81 ± 12.6	77.56 ± 15.8	76.03 ± 15.1
	60-60	95.41 ± 0.3	77.70 ± 3.1	77.87 ± 3.4	77.64 ± 1.5
Descending	365-12	93.49 ± 0.8	73.38 ± 5.9	58.90 ± 9.7	65.50 ± 7.1
	240-12	93.44 ± 0.7	70.48 ± 5.9	64.34 ± 4.9	67.25 ± 3.1
	120-12	93.85 ± 0.8	73.49 ± 6.3	64.51 ± 4.6	68.04 ± 2.8
	60-12	93.81 ± 1.2	75.99 ± 9.2	61.69 ± 5.9	67.00 ± 4.0
	12-12	92.56 ± 0.6	68.10 ± 6.0	53.91 ± 5.1	61.66 ± 2.4
	24-24	93.80 ± 0.9	72.71 ± 6.9	66.29 ± 4.3	69.28 ± 3.1
	60-24	93.67 ± 1.2	72.52 ± 7.8	67.71 ± 6.1	68.89 ± 5.1
	48-48	95.37 ± 0.3	79.38 ± 3.6	75.53 ± 3.4	76.93 ± 1.2
	60-48	94.83 ± 0.3	74.77 ± 3.5	76.48 ± 4.1	75.23 ± 1.5
	60-60	95.30 ± 0.6	78.58 ± 5.49	75.98 ± 4.1	76.88 ± 1.7

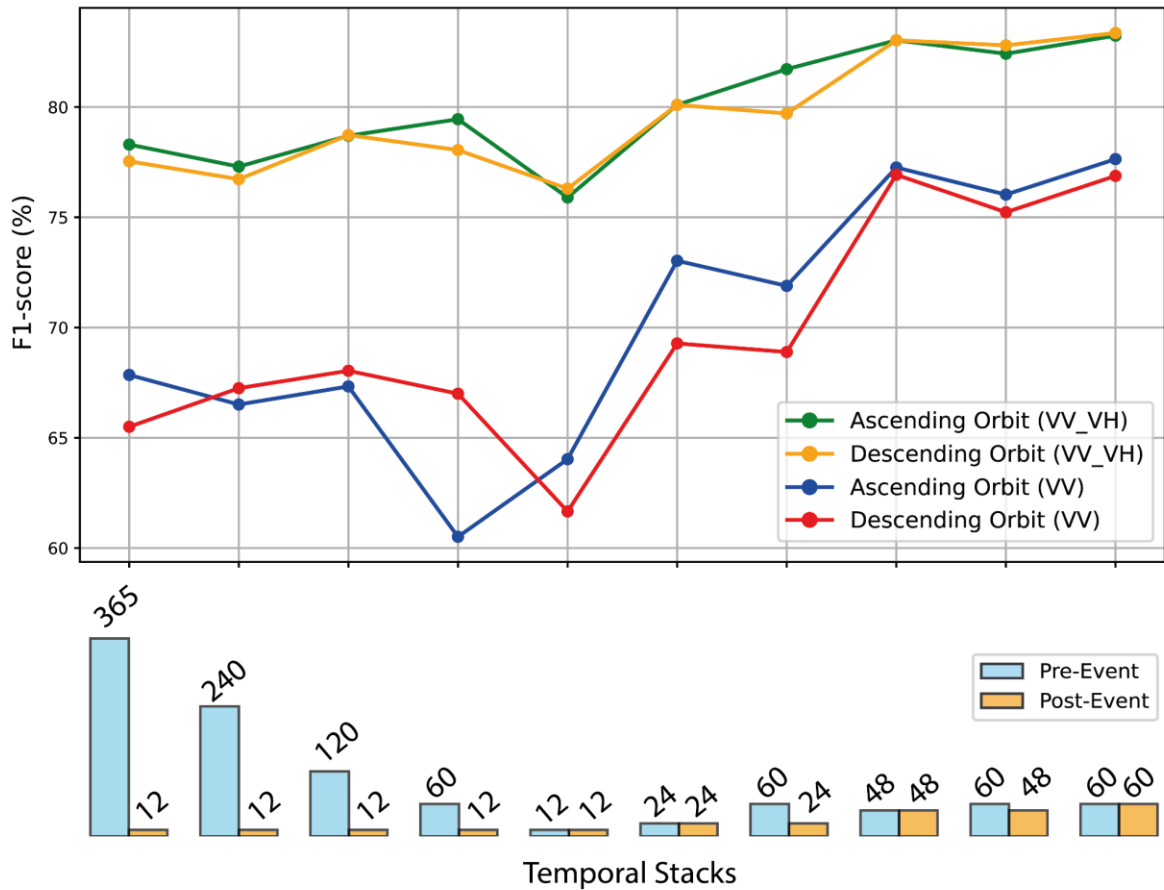


Figure 3: Performance of models trained on different pre- and post-event temporal stacks, considering both ascending and descending orbits and utilizing VV and VV_VH data combinations. The x-axis represents the variation in the pre-event stack dimension across the first five temporal stacks, while the post-event stack remains constant at 12, accommodating a single acquisition per acquisition geometry. This variation elucidates how model performance changes concerning the pre-event stack dimension. The remaining stacks extend the analysis by increasing also the post-event dimension.

5.2 Landslide rapid assessment on unseen MLEs

In this section, we present the detection results of the models that demonstrated the best rapid assessment performance for both descending and ascending orbits separately. The characteristics of the hyperparameters and performance of the models used in the rapid assessment are available in Table 6. Specifically, we showcase results for the Sumatra study case in Figure 4 which has not been included in the training. We focus on the VV_VH combination, and in Figure 5 with the VV combination. Additionally, we provide further examples in the Haiti MLE, which are available in Figure 6. For deeper insights into XAI, pixel contributions are elaborated in Figure 7.

Table 6: Hyperparameters and performance of the models used for rapid assessment, considering both VV and VV_VH combinations, for both ascending and descending orbits. All models utilize a pre-event stack of 60 days and a post-event stack of 12 days, with a fixed learning rate of 0.001. Note that the scores for the VV combinations may appear lower due to the inclusion of data from additional study cases (Gorka, Kaikoura, and Capellades), which aims to enhance the generalizability of the models. Consequently, lower scores in this context do not necessarily indicate lower overall performance compared to the models presented in Table 5.

Name	Orbit	Train imbalance	Filters	Dropout rate	Accuracy (%)	Precision (%)	Recall (%)	F1-score (%)
VV_VH	Ascending	6	32	0.7	96.49	85.73	79.75	82.63
	Descending	5	64	0.5	96.12	86.27	74.91	80.19
VV	Ascending	5	64	0.5	90.88	52.55	63.02	57.31
	Descending	5	32	0.7	93.18	69.12	57.61	62.84

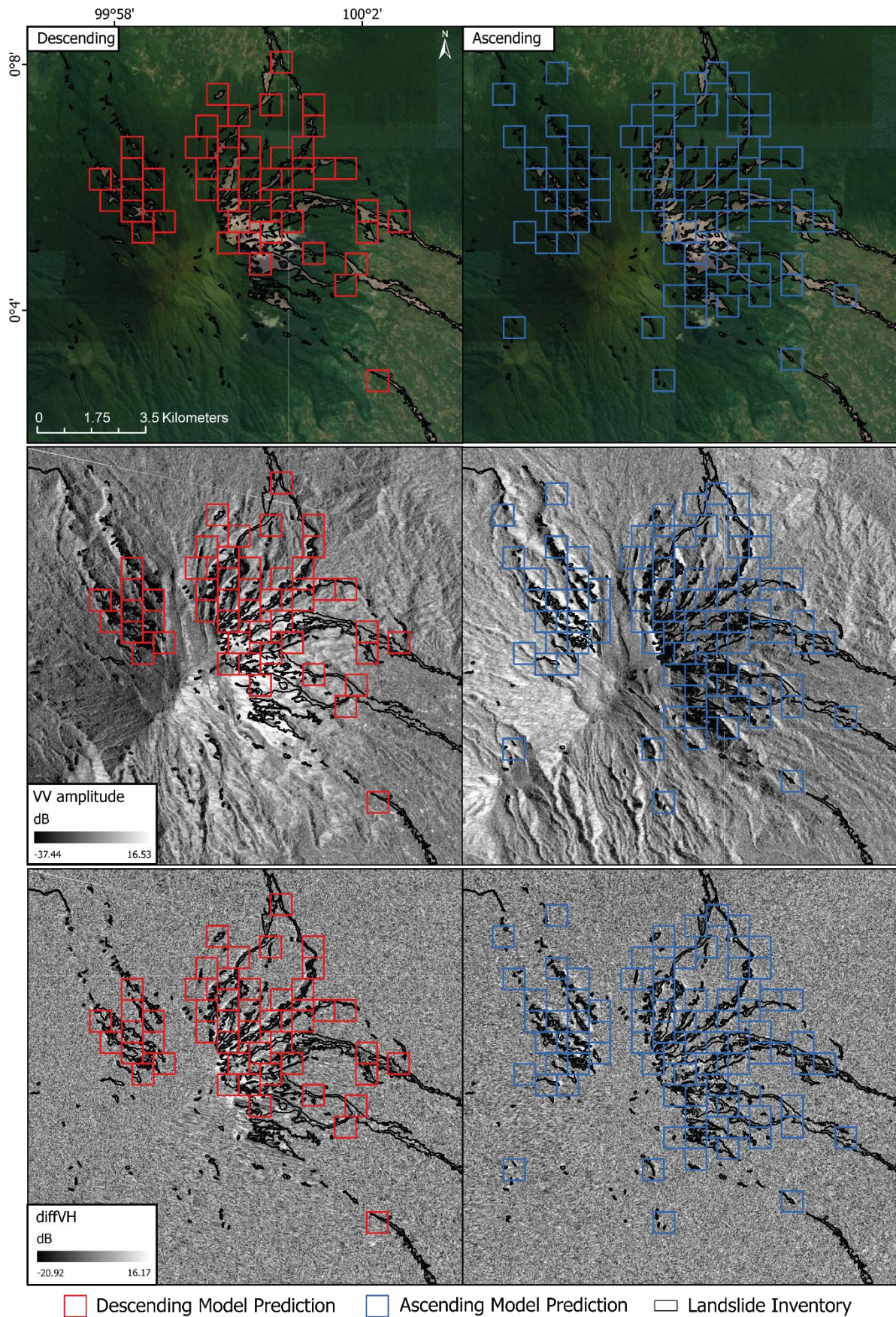


Figure 4: Rapid assessment for the 2022 Sumatra event utilizing VV_VH combination and 60-12 stack pre- and post-event. This unseen event validates the comprehensive generalizability in the rapid assessment of the VV_Vh-

based detection models. The left column shows the predictions obtained using the descending orbit, while the right shows the predictions based on the ascending orbit.

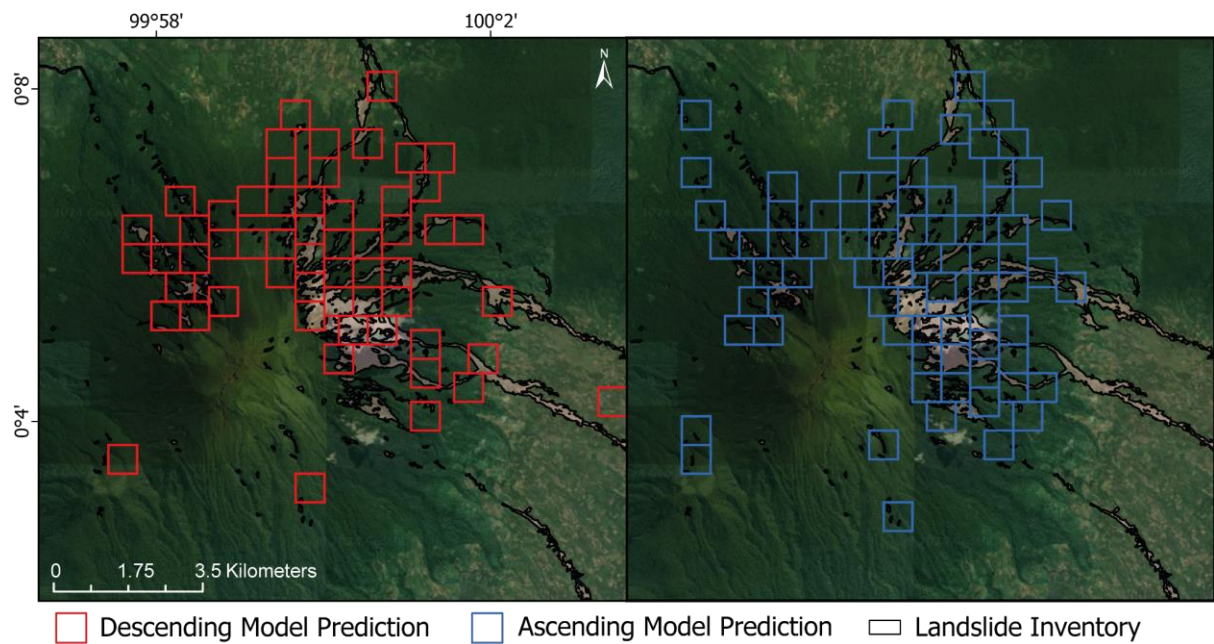


Figure 5: Rapid assessment for the 2022 Sumatra event utilizing VV combination trained on all the available study areas and 60-12 stack pre- and post-event. This unseen event validates the comprehensive generalizability in the rapid assessment of the VV-based detection models. The left column shows the predictions obtained using the descending orbit, while the right shows the predictions based on the ascending orbit.

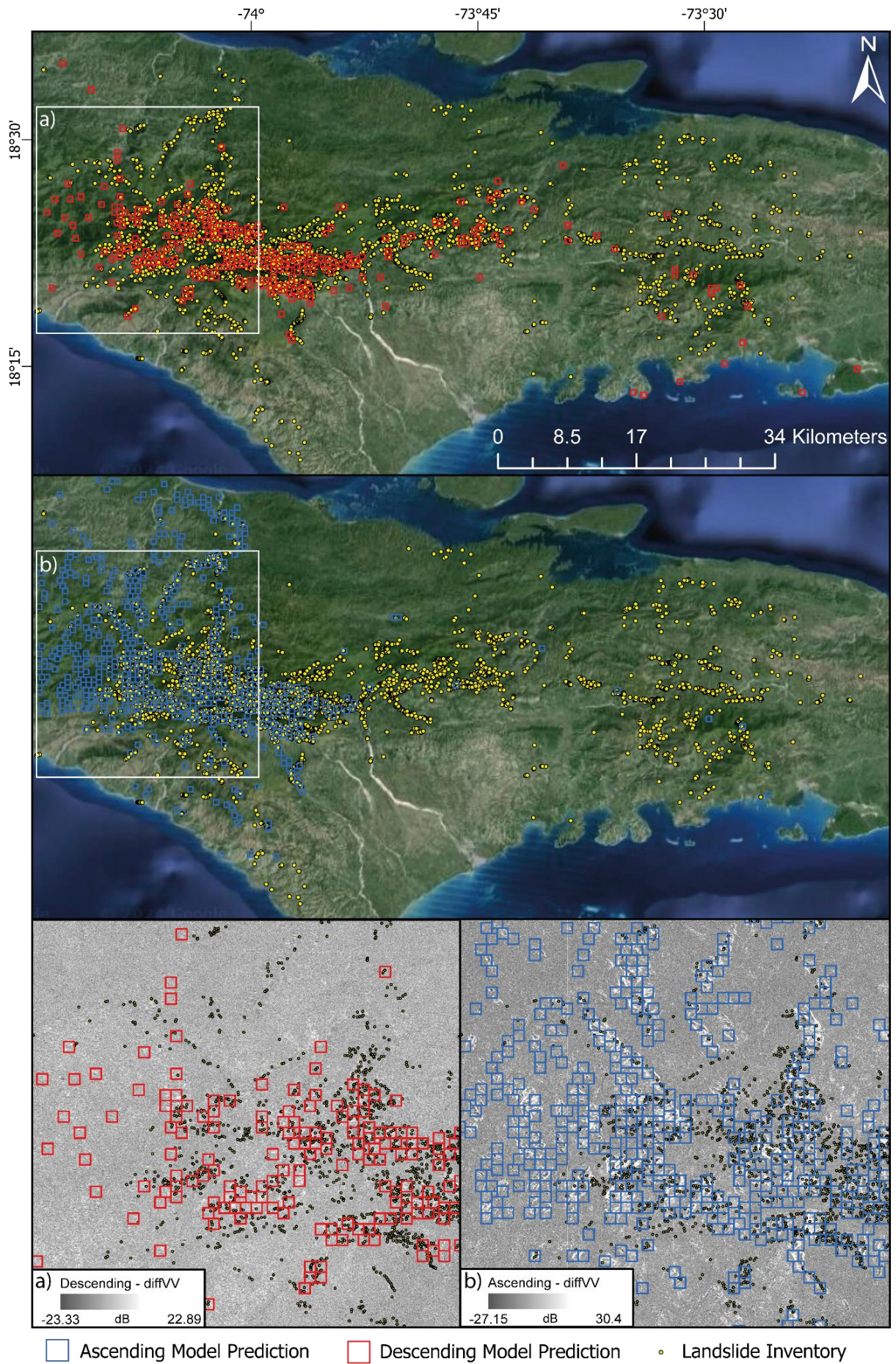


Figure 6: This figure presents the rapid assessment conducted for the 2021 Haiti event, utilizing the VV_VH combination and the 60-12 stack of pre- and post-event imagery, for both ascending and descending orbits. This unseen event serves as a validation of the comprehensive generalizability of the proposed models. Figures (a) and (b) depict the areas where the ascending model tends to overpredict the landslide class (FP) compared to descending-based predictions. Here the background is represented as diffVV, highlighting significant differences between pre and post-event imagery, particularly pronounced in areas susceptible to foreshortening effects in the ascending imagery.

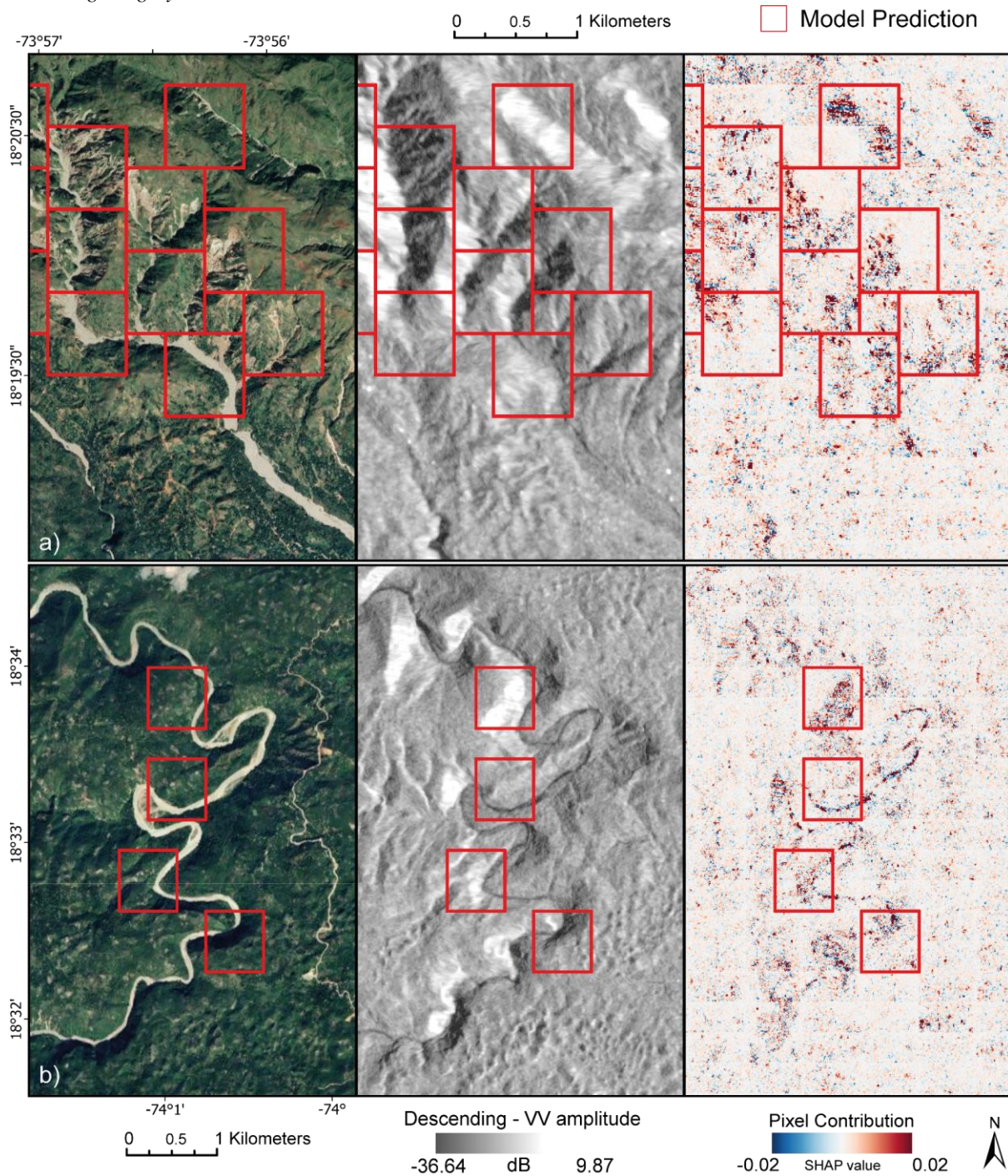


Figure 7: Prediction results for the 2021 Haiti event were generated using the VV_VH combination and a 60-60 stack pre- and post-event, descending orbit. a) True Positives; b) False Positives. The figure shows orthophoto, post-event VV amplitude, and Pixel Contribution (SHAP value) to derive the final detection. Notably, SHAP values represent the mean of the pixel contribution across all four bands in the image. It's important to highlight that the pixel contribution is calculated for all regions of interest (ROIs) during prediction. However, not all ROIs are

identified as landslides. The visualization depicts red clusters representing areas that increase the probability of a certain ROI being classified as landslides, while blue clusters signify the opposite effect.

6. Discussion

6.1 Comparison with Existing Landslide Rapid Assessment Tools

Few existing landslide rapid assessment tools are readily deployable in case of new MLEs: Meena et al. (2023), and those scrutinized by Amatya et al. (2023) encompassing both optical and SAR-based landslide rapid assessment approaches (Handwerger et al. 2022).

The SAR-based rapid assessment tool implemented by Amatya et al. (2023) stands out for its direct applicability to new events, making it closely aligned with our research objectives. Hence, we draw a direct comparison with their methodology. While their method focuses on all surface changes and does not consider SAR geometric distortions, ours specifically targets landslide-related alterations. This distinction is crucial because post-earthquake amplitude alterations can stem from various factors besides landslides. Additionally, the combination of data from both ascending and descending orbits in Amatya inevitably includes geometric distortions arising from the two viewing angles. This integration can significantly compromise the accurate detection of specific features in mountainous areas, such as slope failures. For instance, calculating the median of certain pixels may inadvertently include areas affected by layover in one orbit and foreshortening in the other. Finally, we note that our models' performance does not enhance with an increase in the number of pre-event temporal stacks, which contrasts with the findings reported by Handwerger et al. (2022). Furthermore, augmenting the pre-event stack while keeping the post-event stack constant drops the quality of the result. This might be due to the asymmetry in sampling the physical processes that occur in the different stacks.

Other rapid assessment tools, such as those developed by Meena et al. (2023) and other methods evaluated by Amatya et al. (2023), such as HazMapper (Scheip and Wegmann, 2021), and ALADIM (Deprez et al., 2022), rely on optical data and employ diverse techniques, including object-based image analysis (OBIA) (Blaschke, 2010) and DL segmentation models. These approaches excel at accurately outlining landslide boundaries. Generally, optical-based tools are deemed more precise than SAR-based methods due to the inherent characteristics of the latter. However, there exists a trade-off: while optical techniques offer superior precision, they are hindered by limitations like cloud cover and daylight dependency (Nava et al., 2022b) and can therefore be of no use or benefit during disaster response when the rapid access to landslide inventories is key information for first emergency responders. Conversely, SAR-based methods like ours yield predictions regardless of weather conditions or time of day, albeit with potential sacrifices in accuracy.

6.2 Insights by Spatial XAI

XAI plays a crucial role in SAR data analysis, especially due to its less intuitive nature compared to optical imagery. XAI offers invaluable insights into patch classification tasks by revealing pixel contributions to the model's decisions on a per-patch basis. This detailed analysis uncovers spurious relationships and clarifies the features the model focuses on during decision-making. Leveraging XAI provides key insights into how the model distinguishes between *landslides* and *non-landslides*. Figure 8 illustrates concrete examples of pixel contributions. Within these examples, we present four patches where the model assigns a high probability (0.87) of belonging to the landslide class in two instances. While post-event VV imagery maintains this emphasis, post-event VH imagery often shows pixels contributing to increased landslide probability without displaying the landslides themselves. This pattern persists across all VH band cases, suggesting the model uses VH for contextual insights. Despite VV and VH having minor weights in the final model output, they play crucial roles when combined with more impactful features like $diffVV$ and $diffVH$. Understanding the model's overall interactions and decision-making remains challenging due to the nonlinear coupling effects of positive and negative values of SHAP is essential, as lower peak values in the first two bands can still influence detection results. Consequently, the model's decision-making can vary significantly from case to case. Figure 8c illustrates a scenario where the size of the landslide is not enough to produce a distinct signature in the SAR image, resulting in an indistinguishable from the speckle-like "salt and pepper" effect with minimal changes in dimensions, shape, and backscatter. In such cases, the model struggles to correctly classify the patch and assigns a very low probability (0.14) of containing a landslide, despite the presence of multiple landslides within the area. Moreover, while we meticulously filter the

inventory to exclude landslides occurring in areas affected by shadow and layover, we still encounter situations where landslides are present within these regions, resulting in bias in the training phase and misclassification (e.g., Figure 8d). This challenge stems from our method of calculating distortion masks, which relies on the geometric interplay between the satellite's side view and the terrain, represented by the SRTM 30m resolution DEM.

Overall, the pixel contributions associated with the *diffVV* and *diffVH* bands are promising, as the model demonstrates an ability to identify the areas where most of the landslides occur and focuses attention on the landslide-related pixels. It may be worthwhile to explore applying unsupervised clustering techniques to precisely locate these landslides within the predicted landslide patches. However, it is important to note that the location of landslide-related information in SAR imagery does not always align with the location of landslides in optical imagery due to geometric distortions, which is a current inherent limitation of SAR satellite data.

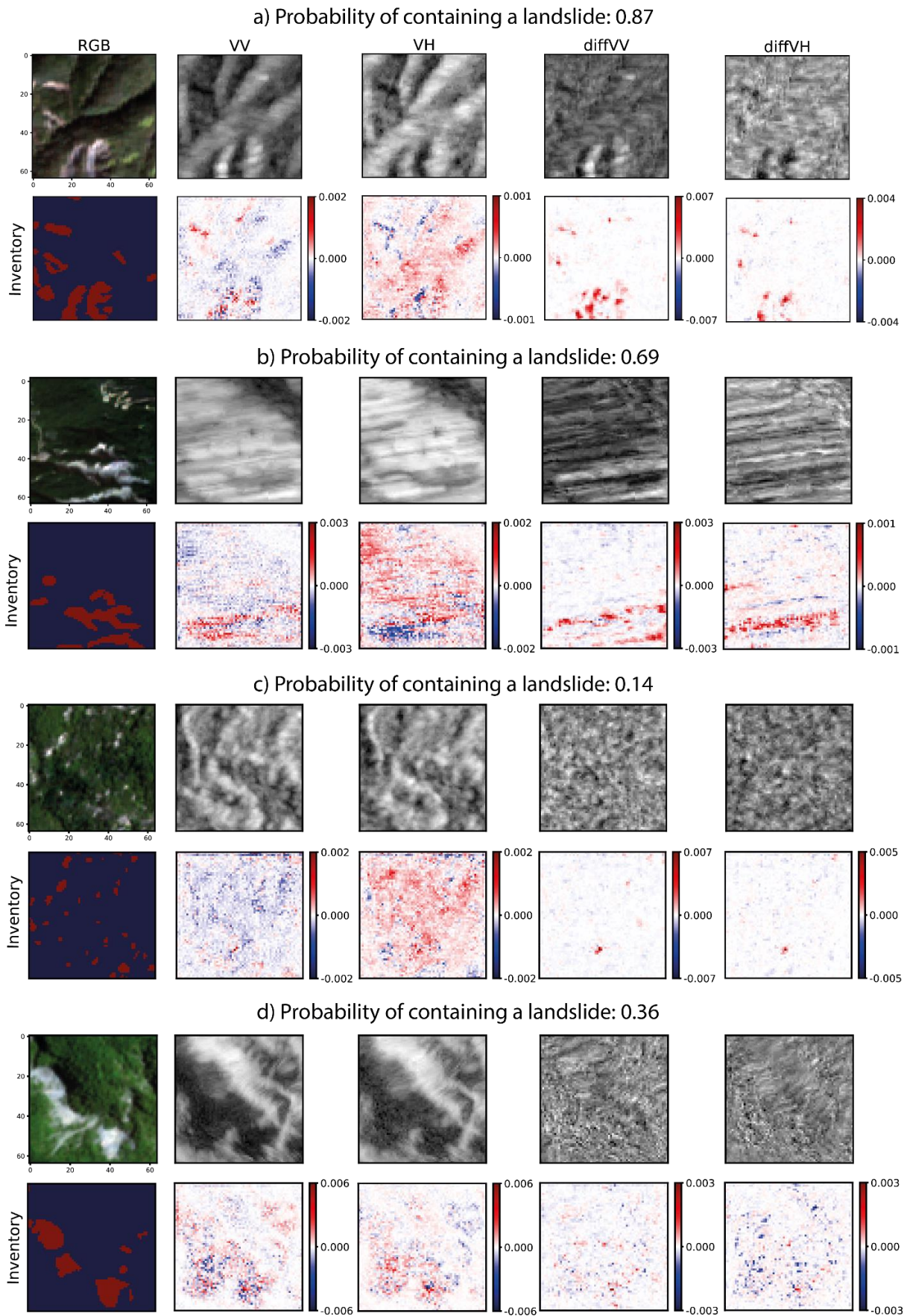


Figure 8: XAI pixel contribution maps. We showcase pixel contributions for each of the bands in the patches, alongside a true color image, SAR bands, landslide inventory, and SHAP pixel contributions for four patches

within the mixed test set. a) and b) depict true positives, where a) exemplifies a distinguishable landslide correctly detected with a high probability of belonging to the landslide class, while b) showcases landslides accurately classified despite foreshortening effects. In contrast, c) and d) represent false negatives. In c), landslides are undetected due to their small individual dimensions, illustrating a limitation of the model. d) illustrates another case of undetected landslides, attributed to missing information in the SAR images.

6.3 Supporting Arguments

Our proposed method demonstrates generalization capabilities, performing well across diverse landscapes and geographical locations. Our approach partially utilizes GEE for data pre-processing, thus resolving the need for specialized GIS software. However, depending on the dimensions of the areas our model predicts, a minimum level of hardware is necessary to support the deployment of our models. An alternative solution could be to leverage cloud computing capabilities such as Google Colaboratory (Yang et al., 2023). With minimal missed detections and overpredictions, it proves reliable even when faced with previously unseen landslide events during rapid assessment tasks. We ensure its robustness and adaptability by training and evaluating the model across areas exhibiting a wide range of landslide occurrences and environmental variations, including distinct terrains and events. The purpose of our new sampling technique is not to introduce a priori noise and biases caused by landslides located in layover and shadowing areas. By using this method, we can train the model using obvious landslide patches, thereby attempting to minimize the effect of sampling in mountainous regions where SAR data frequently show geometric distortions (Burrows et al., 2020). In situations where landslide information is not clearly represented in the SAR data, the model may erroneously associate specific distortions or features with landslide occurrences. By incorporating such filtering techniques during the sampling process, we mitigate this risk by ensuring that the model focuses only on genuine landslide indicators present in the SAR imagery.

We also provide the SAR-LRA Tool in its Beta version. This tool stands as an important asset for swift all-weather day-night landslide assessment after earthquake-triggered MLEs, furnishing disaster operators with insights for timely disaster management. Furthermore, as reliable inventories become available, we pledge to continually update and refine the models, ensuring their generalizability to diverse terrains and MLE types to increase with time.

6.4 Problems and Gap Analysis

We have tested the method in a variety of environments, all of which are mainly vegetated (see Figure A1). In all the study areas, the method has proven to be effective. However, it is important to note that there may be different environments where the method may not perform as well. While we utilize indicators such as changes in differential maps, uncertainty arises when these changes occur for reasons not directly associated with landslides (Figure 7b), such as water level and/or suspended material changes (Hertel et al., 2023). This uncertainty becomes particularly evident when our methodology fails to yield satisfactory results, as demonstrated by our experiences in the ascending orbit in Haiti. However, this challenge could be mitigated if an expert examines the images beforehand and understands that the observed changes may be influenced by anomalous pre-processing outputs or geometric acquisition issues. By removing the anomalous images from the stack, the results return to normal, highlighting the importance of careful preprocessing and quality control.

Additionally, the absence or minimal influence of snow in the training and calibration areas may disrupt our detection capabilities (see Figure A1), especially in regions where snow cover is present before, during, and/or right after the MLE. Another limitation lies in the model's inability to effectively detect small landslides, primarily due to Sentinel-1 data resolution constraints. Utilizing higher-resolution imagery would significantly enhance prediction accuracy. While the 5% threshold set during training helps minimize overpredictions and excludes patches lacking landslide-related information in SAR images, it may overlook small landslides, particularly if their signals are weak or if only one small landslide is present in the area. Furthermore, our methodology cannot differentiate between different types of landslides, as such information is often unavailable in the inventories used for our research. Continuous testing is essential for mitigating uncertainties associated with unknown and unexplored terrains, poor image quality, and the presence of snow. Due to the methodology employed, conducting a sensitivity analysis on both landslide dimensions and model performance is unfeasible. This is primarily because a single patch often encompasses multiple landslide occurrences. The models have no apparent bias given by the landcover within the areas tested (see Figure A2). However, we observed a discrepancy in the distribution of slope

and aspect values when comparing the pixels within landslide scars of patches correctly predicted as landslides (TP) with those where landslides were missed (FN). In TP cases, the distributions of slope and aspect align with the overall distribution observed in landslide scars across the entire training set (see Figure A1). However, considering FN, the distributions diverge, particularly in areas with high slope degrees, which can increase the SAR backscatter distortions (see Figure 9). Additionally, in the aspect, we observe that misclassifications exhibit a peak around 160° (SE) for the descending orbit, whereas the distribution of TP remains consistent with the overall distribution, with the main peak occurring around 225° (SW). Observations indicate that the model is less likely to detect landslides occurring on slopes exceeding 30° and within the aspect range of 100° to 200° . This aspect range is related to the Sentinel-1 descending orbit view.

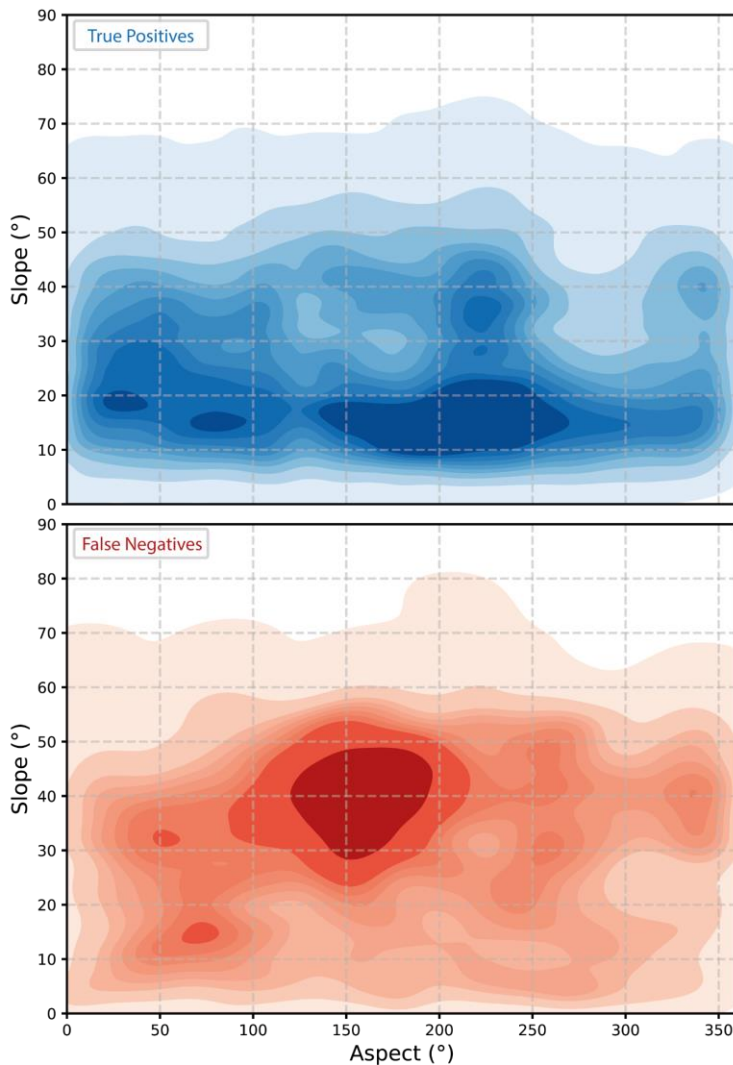


Figure 9: Kernel Density Estimation (KDE) of the Slope and Aspect values in the landslide scars, in the True Positive and False Negative predictions of the test dataset by the model trained on descending orbit for the 60_12 temporal stack combination in the six study areas used to perform the SAR settings comparison.

6.5 Future Research Directions

Our analysis was limited to earthquake-induced MLEs. Future research will expand to include rainfall-triggered landslides as well. Furthermore, our analysis focused exclusively on SAR backscatter intensity using the C-band Sentinel-1 satellite. However, our methodology can be reproduced just or coupled with imagery from SAR satellites operating with different radar wavelengths and resolutions, such as X and L-bands. Future SAR missions, such as NASA and ISRO's SAR initiative (NISAR), operating with S- and L-band sensors, are anticipated to offer enhanced capabilities, particularly in vegetated regions and higher acquisition frequencies. The utilization of different wavelengths and/or polarizations could potentially provide valuable additional information, likely leading to improved performance of our models. Testing these new data would be highly intriguing, as they have the potential to enrich our understanding and further refine our methodologies for landslide

detection. Exploring an alternative approach, we could begin directly from the Single Look Complex (SLC) imagery and incorporate custom filtering and coregistration techniques. This approach offers greater flexibility in creating SAR composites, enabling us to experiment with various combinations of data. For example, we could assess the performance by including differenced coherence, despite the potential decrease in spatial resolution. While coherence is known for its higher sensitivity to changes compared to backscatter (Burrows), its inclusion may not directly enhance detection performance, but it presents a promising avenue for future investigations.

7. Summary

In this study, we showcase with our results the efficacy of Sentinel-1 SAR backscatter and DNNs for one-shot rapid landslide detection in all-weather and day-night conditions. We develop this method by using 11 earthquake-induced MLEs, comprising a total of 73 thousand landslides. We test the approach on unseen MLEs, located in Sumatra and Haiti, to validate the generalizability and applicability of the approach. We use XAI to examine the pixel contributions of the model across various SAR bands, uncovering indicators of landslide-related information, also in foreshortening. As per our current knowledge, this study represents the first evidence supporting the feasibility of applying DNNs to enable one-shot landslide rapid assessment via SAR backscatter data, across diverse geographic locations. Therefore, we establish a robust foundation for future research endeavors, wherein SAR and DNNs can be harnessed to locate terrain changes in mountainous regions. The approach leverages the cloud-based GIS capabilities of GEE, eliminating the need for specialized software and democratizing geospatial analysis globally. The approach offers distinct advantages over optical-based methods, particularly in its resilience to adverse weather conditions. Our analysis reveals that change detection bands, specifically *diffVV* and *diffVH*, demonstrate greater discriminative weight and a higher potential to delineate the landslide body, than backscatter alone. Lastly, we introduce the SAR-LRA Tool in its Beta version, serving as an asset for swift all-weather landslide assessment. As reliable inventories become increasingly available, we are committed to continuously updating and refining our models and datasets to improve their accuracy and generalizability.

Given the frequent incidence of MLEs, the development of a robust modeling approach is imperative to timely assess the spatial distribution of these phenomena. This research will pave the way for efficient rapid assessment of MLEs in the future.

8. Data and Code Availability Statement

The code and model weights of SAR-LRA are available at <https://github.com/lorenzonava96/SAR-and-DL-for-Landslide-Rapid-Assessment>. As new MLE polygon inventories emerge, we will update the tool accordingly and upload the new versions in the same repository, accompanied by detailed descriptions of the modifications made.

Acknowledgments

The inventories utilized in our analysis primarily originate from open-access repositories, with a notable emphasis on the “Landslide Inventories” repository provided by USGS (accessible at <https://www.sciencebase.gov/catalog/item/586d824ce4b0f5ce109fc9a6>). We extend our sincere appreciation to the authors for their generous contribution of data, which greatly facilitated our research efforts. This research was supported by the “The Geosciences for Sustainable Development” project (Budget Ministero dell’Università e della Ricerca–Dipartimenti di Eccellenza 2023–2027C93C23002690001). Novellino was funded through the BGS International NC programme ‘Geoscience to tackle Global Environmental Challenges’, NERC reference NE/X006255/1. Monserrat was funded by the Spanish Grant PID2020-116540RB-C21 funded by MCIN/AEI /10.13039/501100011033.

References

- Abadi, M., Agarwal, A., Barham, P., Brevdo, E., Chen, Z., Citro, C., Corrado, G.S., Davis, A., Dean, J., Devin, M., 2016. Tensorflow: Large-scale machine learning on heterogeneous distributed systems. arXiv preprint arXiv:1603.04467.
- Aimaiti, Y., Liu, W., Yamazaki, F., Maruyama, Y., 2019. Earthquake-induced landslide mapping for the 2018 Hokkaido Eastern Iburi earthquake using PALSAR-2 data. *Remote Sens (Basel)* 11. <https://doi.org/10.3390/rs11202351>
- Amatya, P., Scheip, C., Déprez, A., Malet, J.-P., Slaughter, S.L., Handwerger, A.L., Emberson, R., Kirschbaum, D., Jean-Baptiste, J., Huang, M.-H., Clark, M.K., Zekkos, D., Huang, J.-R., Pacini, F., Boissier, E., 2023. Learnings from rapid response efforts to remotely detect landslides triggered by the August 2021 Nippes earthquake and Tropical Storm Grace in Haiti. *Natural Hazards* 118, 2337–2375. <https://doi.org/10.1007/s11069-023-06096-6>
- Antonello, G., Casagli, N., Farina, P., Leva, D., Nico, G., Sieber, A.J., Tarchi, D., 2004. Ground-based SAR interferometry for monitoring mass movements. *Landslides* 1, 21–28. <https://doi.org/10.1007/s10346-003-0009-6>
- Basofi, A., Fariza, A., Dzulkarnain, M.R., 2016. Landslides susceptibility mapping using fuzzy logic: A case study in Ponorogo, East Java, Indonesia, in: 2016 International Conference on Data and Software Engineering (ICoDSE). IEEE, pp. 1–7. <https://doi.org/10.1109/ICODSE.2016.7936156>
- Beni, T., Nava, L., Gigli, G., Frodella, W., Catani, F., Casagli, N., Gallego, J.I., Margottini, C., Spizzichino, D., 2023. Classification of rock slope cavernous weathering on UAV photogrammetric point clouds: The example of Hegra (UNESCO World Heritage Site, Kingdom of Saudi Arabia). *Eng Geol* 325. <https://doi.org/10.1016/j.enggeo.2023.107286>
- Bhuyan, K., Rana, K., Ferrer, J. V., Cotton, F., Ozturk, U., Catani, F., Malik, N., 2024. Landslide topology uncovers failure movements. *Nat Commun* 15, 2633. <https://doi.org/10.1038/s41467-024-46741-7>
- Bhuyan, K., Tanyaş, H., Nava, L., Puliero, S., Meena, S.R., Floris, M., van Westen, C., Catani, F., 2023. Generating multi-temporal landslide inventories through a general deep transfer learning strategy using HR EO data. *Sci Rep* 13, 162. <https://doi.org/10.1038/s41598-022-27352-y>
- Blaschke, T., 2010. Object based image analysis for remote sensing. *ISPRS Journal of Photogrammetry and Remote Sensing* 65, 2–16. <https://doi.org/10.1016/j.isprsjprs.2009.06.004>
- Burrows, K., Walters, R.J., Milledge, D., Densmore, A.L., 2020. A systematic exploration of satellite radar coherence methods for rapid landslide detection. *Natural Hazards and Earth System Sciences* 20, 3197–3214. <https://doi.org/10.5194/nhess-20-3197-2020>
- Burrows, K., Walters, R.J., Milledge, D., Spaans, K., Densmore, A.L., 2019. A New Method for Large-Scale Landslide Classification from Satellite Radar. *Remote Sens (Basel)* 11, 237. <https://doi.org/10.3390/rs11030237>
- Catani, F., 2021. Landslide detection by deep learning of non-nadir and crowdsourced optical images. *Landslides* 18. <https://doi.org/10.1007/s10346-020-01513-4>
- Catani, F., Casagli, N., Ermini, L., Righini, G., Menduni, G., 2005. Landslide hazard and risk mapping at catchment scale in the Arno River basin. *Landslides* 2, 329–342. <https://doi.org/10.1007/s10346-005-0021-0>
- Chorowicz, J., Scanvic, J.Y., Rouzeau, O., Cuervo, G.V., 1998. Observation of recent and active landslides from SAR ERS-1 and JERS-1 imagery using a stereo-simulation approach: Example of the Chicamocha valley in Colombia. *Int J Remote Sens* 19, 3187–3196. <https://doi.org/10.1080/014311698214253>
- Dai, L., Fan, X., Wang, X., Fang, C., Zou, C., Tang, X., Wei, Z., Xia, M., Wang, D., Xu, Q., 2023a. Coseismic landslides triggered by the 2022 Luding Ms6.8 earthquake, China. *Landslides* 20, 1277–1292. <https://doi.org/10.1007/s10346-023-02061-3>
- Dai, L., Fan, X., Wang, X., Fang, C., Zou, C., Tang, X., Wei, Z., Xia, M., Wang, D., Xu, Q., 2023b. Coseismic landslides triggered by the 2022 Luding Ms6.8 earthquake, China. *Landslides* 20, 1277–1292. <https://doi.org/10.1007/s10346-023-02061-3>
- Del Soldato, M., Solari, L., Novellino, A., Monserrat, O. and Raspini, F., 2021. A new set of tools for the generation of InSAR visibility maps over wide areas. *Geosciences*, 11(6), p.229. <https://doi.org/10.3390/geosciences11060229>

Deprez, A., Marc, O., Malet, J. P., Stumpf, A., & Michéa, D. (2022, May). ALADIM-A change detection on-line service for landslide detection from EO imagery. In EGU General Assembly Conference Abstracts (pp. EGU22-3536).

Esposito, G., Marchesini, I., Mondini, A.C., Reichenbach, P., Rossi, M., Sterlacchini, S., 2020. A spaceborne SAR-based procedure to support the detection of landslides. *Natural Hazards and Earth System Sciences* 20, 2379–2395. <https://doi.org/10.5194/nhess-20-2379-2020>

Fang, C., Fan, X., Zhong, H., Lombardo, L., Tanyas, H., Wang, X., 2022. A Novel Historical Landslide Detection Approach Based on LiDAR and Lightweight Attention U-Net. *Remote Sens (Basel)* 14, 4357. <https://doi.org/10.3390/rs14174357>

Ferrario, M.F., 2019. Landslides triggered by multiple earthquakes: insights from the 2018 Lombok (Indonesia) events. *Natural Hazards* 98. <https://doi.org/10.1007/s11069-019-03718-w>

Froude, M.J., Petley, D.N., 2018. Global fatal landslide occurrence from 2004 to 2016. *Natural Hazards and Earth System Sciences* 18, 2161–2181. <https://doi.org/10.5194/nhess-18-2161-2018>

García-Delgado, H., Chaparro Cordón, J. L., & Gamboa Rodríguez, C. A. (2021). Landslides triggered by the December 24, 2019 Mesetas (Meta, Colombia) Earthquake. In *Proceedings of the 13th International Symposium on Landslides*.

Ghorbanzadeh, O., Blaschke, T., Gholamnia, K., Meena, S.R., Tiede, D., Aryal, J., 2019. Evaluation of different machine learning methods and deep-learning convolutional neural networks for landslide detection. *Remote Sens (Basel)* 11. <https://doi.org/10.3390/rs11020196>

Guzzetti, F., Mondini, A.C., Cardinali, M., Fiorucci, F., Santangelo, M., Chang, K.-T., 2012. Landslide inventory maps: New tools for an old problem. *Earth Sci Rev* 112, 42–66. <https://doi.org/10.1016/j.earscirev.2012.02.001>

Han, Z., Fang, Z., Li, Y., Fu, B., 2023. A novel Dynahead-Yolo neural network for the detection of landslides with variable proportions using remote sensing images. *Front Earth Sci (Lausanne)* 10. <https://doi.org/10.3389/feart.2022.1077153>

He, K., Tanyas, H., Chang, L., Hu, X., Luo, G., Lombardo, L., 2023. Modelling InSAR-derived hillslope velocities with multivariate statistics: A first attempt to generate interpretable predictions. *Remote Sens Environ* 289, 113518. <https://doi.org/10.1016/j.rse.2023.113518>

Hertel, V., Chow, C., Wani, O., Wieland, M., Martinis, S., 2023. Probabilistic SAR-based water segmentation with adapted Bayesian convolutional neural network. *Remote Sens Environ* 285, 113388. <https://doi.org/10.1016/j.rse.2022.113388>

Hu, K., Zhang, X., You, Y., Hu, X., Liu, W., Li, Y., 2019. Landslides and dammed lakes triggered by the 2017 Ms6.9 Milin earthquake in the Tsangpo gorge. *Landslides* 16, 993–1001. <https://doi.org/10.1007/s10346-019-01168-w>

Jung, J., Yun, S.-H., 2020. Evaluation of Coherent and Incoherent Landslide Detection Methods Based on Synthetic Aperture Radar for Rapid Response: A Case Study for the 2018 Hokkaido Landslides. *Remote Sens (Basel)* 12, 265. <https://doi.org/10.3390/rs12020265>

Kingma, D.P., Ba, J.L., 2015. Adam: A method for stochastic optimization, in: *3rd International Conference on Learning Representations, ICLR 2015 - Conference Track Proceedings*.

Konishi, T., Suga, Y., 2018. Landslide detection using COSMO-SkyMed images: a case study of a landslide event on Kii Peninsula, Japan. *Eur J Remote Sens* 51, 205–221. <https://doi.org/10.1080/22797254.2017.1418185>

Lee, C.H., Lin, C.R., Chen, M.S., 2001. Sliding-window filtering: An efficient algorithm for incremental mining, in: *International Conference on Information and Knowledge Management, Proceedings*.

Lindsay, E., Frauenfelder, R., Rüther, D., Nava, L., Rubensdotter, L., Strout, J., Nordal, S., 2022. Multi-Temporal Satellite Image Composites in Google Earth Engine for Improved Landslide Visibility: A Case Study of a Glacial Landscape. *Remote Sens (Basel)* 14. <https://doi.org/10.3390/rs14102301>

Lindsay, E.; Jarna Ganerød, A.; Devoli, G.; Reiche, J.; Nordal, S.; Frauenfelder, R.; Tokle, L. Understanding Landslide Expression in SAR Backscatter Data: A Global Study. *Preprints* 2023, 2023020390. <https://doi.org/10.20944/preprints202302.0390.v1>

Lin, T.-Y., Goyal, P., Girshick, R., He, K., Dollar, P., 2017. Focal Loss for Dense Object Detection, in: *2017 IEEE International Conference on Computer Vision (ICCV)*. IEEE, pp. 2999–3007. <https://doi.org/10.1109/ICCV.2017.324>

- Liu, Q., Wu, T., Deng, Y., Liu, Z., 2023. SE-YOLOv7 Landslide Detection Algorithm Based on Attention Mechanism and Improved Loss Function. *Land (Basel)* 12, 1522. <https://doi.org/10.3390/land12081522>
- Manconi, A., Casu, F., Ardizzone, F., Bonano, M., Cardinali, M., De Luca, C., Gueguen, E., Marchesini, I., Parise, M., Vennari, C., Lanari, R., Guzzetti, F., 2014. Brief Communication: Rapid mapping of landslide events: the 3 December 2013 Montescaglioso landslide, Italy. *Natural Hazards and Earth System Sciences* 14, 1835–1841. <https://doi.org/10.5194/nhess-14-1835-2014>
- Martinez, S.N., Allstadt, K.E., Slaughter, S.L., Schmitt, R., Collins, E., Schaefer, L.N., and Ellison, S., 2021, Landslides triggered by the August 14, 2021, magnitude 7.2 Nippes, Haiti, earthquake: U.S. Geological Survey Open-File Report 2021–1112, 17 p., <https://doi.org/10.3133/ofr20211112>.
- Meena, S.R., Ghorbanzadeh, O., van Westen, C.J., Nachappa, T.G., Blaschke, T., Singh, R.P., Sarkar, R., 2021. Rapid mapping of landslides in the Western Ghats (India) triggered by 2018 extreme monsoon rainfall using a deep learning approach. *Landslides* 18, 1937–1950. <https://doi.org/10.1007/s10346-020-01602-4>
- Meena, S.R., Nava, L., Bhuyan, K., Puliero, S., Soares, L.P., Dias, H.C., Floris, M., Catani, F., 2023. HR-GLDD: a globally distributed dataset using generalized deep learning (DL) for rapid landslide mapping on high-resolution (HR) satellite imagery. *Earth Syst Sci Data* 15. <https://doi.org/10.5194/essd-15-3283-2023>
- Meena, Tavakkoli Piralilou, 2019. Comparison of Earthquake-Triggered Landslide Inventories: A Case Study of the 2015 Gorkha Earthquake, Nepal. *Geosciences (Basel)* 9, 437. <https://doi.org/10.3390/geosciences9100437>
- Meyer, F. (2019). Spaceborne Synthetic Aperture Radar: Principles, data access, and basic processing techniques. *Synthetic Aperture Radar (SAR) Handbook: Comprehensive Methodologies for Forest Monitoring and Biomass Estimation*, 21-64
- Mondini, A., 2017. Measures of Spatial Autocorrelation Changes in Multitemporal SAR Images for Event Landslides Detection. *Remote Sens (Basel)* 9, 554. <https://doi.org/10.3390/rs9060554>
- Mondini, A.C., Guzzetti, F., Chang, K.T., Monserrat, O., Martha, T.R., Manconi, A., 2021a. Landslide failures detection and mapping using Synthetic Aperture Radar: Past, present and future. *Earth Sci Rev.* <https://doi.org/10.1016/j.earscirev.2021.103574>
- Mondini, A.C., Guzzetti, F., Chang, K.T., Monserrat, O., Martha, T.R., Manconi, A., 2021b. Landslide failures detection and mapping using Synthetic Aperture Radar: Past, present and future. *Earth Sci Rev.* <https://doi.org/10.1016/j.earscirev.2021.103574>
- Mondini, A., Santangelo, M., Rocchetti, M., Rossetto, E., Manconi, A., Monserrat, O., 2019. Sentinel-1 SAR Amplitude Imagery for Rapid Landslide Detection. *Remote Sens (Basel)* 11, 760. <https://doi.org/10.3390/rs11070760>
- Nava, L., Bhuyan, K., Meena, S.R., Monserrat, O., Catani, F., 2022a. Rapid Mapping of Landslides on SAR Data by Attention U-Net. *Remote Sens (Basel)* 14. <https://doi.org/10.3390/rs14061449>
- Nava, L., Monserrat, O., Catani, F., 2022b. Improving Landslide Detection on SAR Data Through Deep Learning. *IEEE Geoscience and Remote Sensing Letters* 19. <https://doi.org/10.1109/LGRS.2021.3127073>
- Neubeck, A., Van Gool, L., 2006. Efficient Non-Maximum Suppression, in: 18th International Conference on Pattern Recognition (ICPR'06). IEEE, pp. 850–855. <https://doi.org/10.1109/ICPR.2006.479>
- Nocentini, N., Rosi, A., Segoni, S., Fanti, R., 2023. Towards landslide space-time forecasting through machine learning: the influence of rainfall parameters and model setting. *Front Earth Sci (Lausanne)* 11. <https://doi.org/10.3389/feart.2023.1152130>
- Novellino, A., Pennington, C., Leeming, K., Taylor, S., Alvarez, I.G., McAllister, E., Arnhardt, C. and Winson, A., 2024. Mapping landslides from space: A review. *Landslides*, pp.1-12. <https://doi.org/10.1007/s10346-024-02215-x>
- Parker, R.N., Densmore, A.L., Rosser, N.J., de Michele, M., Li, Y., Huang, R., Whadcoat, S., Petley, D.N., 2011. Mass wasting triggered by the 2008 Wenchuan earthquake is greater than orogenic growth. *Nat Geosci* 4, 449–452. <https://doi.org/10.1038/ngeo1154>
- Plank, S., Twele, A., Martinis, S., 2016. Landslide Mapping in Vegetated Areas Using Change Detection Based on Optical and Polarimetric SAR Data. *Remote Sens (Basel)* 8. <https://doi.org/10.3390/rs8040307>
- Poveda, E., Pedraza, P., Velandia, F., Mayorga, E., Plicka, V., Gallovič, F., Zahradník, J., 2022. 2019 Mw 6.0 Mesetas (Colombia) Earthquake Sequence: Insights From Integrating Seismic and Morphostructural Observations. *Earth and Space Science* 9. <https://doi.org/10.1029/2022EA002465>

- Prakash, N., Manconi, A., Loew, S., 2021. A new strategy to map landslides with a generalized convolutional neural network. *Sci Rep* 11, 9722. <https://doi.org/10.1038/s41598-021-89015-8>
- Rana, K., Malik, N., Ozturk, U., 2022. Landsifier v1.0: a Python library to estimate likely triggers of mapped landslides. *Natural Hazards and Earth System Sciences* 22, 3751–3764. <https://doi.org/10.5194/nhess-22-3751-2022>
- Rana, K., Ozturk, U., Malik, N., 2021. Landslide Geometry Reveals its Trigger. *Geophys Res Lett* 48. <https://doi.org/10.1029/2020GL090848>
- Roback, K., Clark, M.K., West, A.J., Zekkos, D., Li, G., Gallen, S.F., Chamlagain, D., Godt, J.W., 2017. The size, distribution, and mobility of landslides caused by the 2015 Mw7.8 Gorkha earthquake, Nepal. *Geomorphology* 301, 121–138. <https://doi.org/10.1016/j.geomorph.2017.01.030>
- Ruiz, P., Rodriguez, N., Valverde, J., Marden, A., Vecchiarelli, L., Seal, D., Jessee, M. ~A. ~N., Hamburger, M. ~W., 2020. A comprehensive catalog of coseismic landslides in Costa Rica: Toward the development of an empirical landslide hazard model., in: *AGU Fall Meeting Abstracts*. pp. NH030-0004.
- Santangelo, M., Cardinali, M., Bucci, F., Fiorucci, F., Mondini, A.C., 2022. Exploring event landslide mapping using Sentinel-1 SAR backscatter products. *Geomorphology* 397, 108021. <https://doi.org/10.1016/j.geomorph.2021.108021>
- Scheip, C.M., Wegmann, K.W., 2021. HazMapper: a global open-source natural hazard mapping application in Google Earth Engine. *Natural Hazards and Earth System Sciences* 21, 1495–1511. <https://doi.org/10.5194/nhess-21-1495-2021>
- Segoni, S., Rossi, G., Rosi, A., Catani, F., 2014. Landslides triggered by rainfall: A semi-automated procedure to define consistent intensity–duration thresholds. *Comput Geosci* 63, 123–131. <https://doi.org/10.1016/j.cageo.2013.10.009>
- Sella, G.F., Dixon, T.H., Mao, A., 2002. REVEL: A model for Recent plate velocities from space geodesy. *J Geophys Res Solid Earth* 107. <https://doi.org/10.1029/2000JB000033>
- Sentinel Online. Revisit and Coverage. Accessed (Online): 12 November 2023. <https://sentinels.copernicus.eu/web/sentinel/user-guides/sentinel-1-sar/revisit-and-coverage>
- Serey, A., Piñero-Feliciangeli, L., Sepúlveda, S.A., Poblete, F., Petley, D.N., Murphy, W., 2019. Landslides induced by the 2010 Chile megathrust earthquake: a comprehensive inventory and correlations with geological and seismic factors. *Landslides*. <https://doi.org/10.1007/s10346-019-01150-6>
- Shi, X., Wu, Y., Guo, Q., Li, N., Lin, Z., Qiu, H., Pan, B., 2023. Fast Mapping of Large-Scale Landslides in Sentinel-1 SAR Images Using SPAUNet. *IEEE J Sel Top Appl Earth Obs Remote Sens* 16, 7992–8006. <https://doi.org/10.1109/JSTARS.2023.3310153>
- Shorten, C., Khoshgoftaar, T.M., 2019. A survey on Image Data Augmentation for Deep Learning. *J Big Data* 6, 60. <https://doi.org/10.1186/s40537-019-0197-0>
- Singhroy, V., 1995. Sar integrated techniques for geohazard assessment. *Advances in Space Research* 15, 67–78. [https://doi.org/10.1016/0273-1177\(95\)00076-Q](https://doi.org/10.1016/0273-1177(95)00076-Q)
- Song, K., Wang, F., Dai, Z., Iio, A., Osaka, O., Sakata, S., 2019. Geological characteristics of landslides triggered by the 2016 Kumamoto earthquake in Mt. Aso volcano, Japan. *Bulletin of Engineering Geology and the Environment* 78. <https://doi.org/10.1007/s10064-017-1097-1>
- Suga, Y., Konishi, T., 2012. Landslide detection using very high-resolution satellite imageries, in: Entekhabi, D., Honda, Y., Sawada, H., Shi, J., Oki, T. (Eds.), . p. 852428. <https://doi.org/10.1117/12.976033>
- Tang, X., Liu, M., Zhong, H., Ju, Y., Li, W., Xu, Q., 2021. MILL: Channel Attention–based Deep Multiple Instance Learning for Landslide Recognition. *ACM Transactions on Multimedia Computing, Communications, and Applications* 17, 1–11. <https://doi.org/10.1145/3454009>
- Tanyaş, H., Görüm, T., Fadel, I., Yıldırım, C., Lombardo, L., 2022a. An open dataset for landslides triggered by the 2016 Mw 7.8 Kaikōura earthquake, New Zealand. *Landslides* 19, 1405–1420. <https://doi.org/10.1007/s10346-022-01869-9>
- Tanyaş, H., Hill, K., Mahoney, L., Fadel, I., Lombardo, L., 2022b. The world’s second-largest, recorded landslide event: Lessons learnt from the landslides triggered during and after the 2018 Mw 7.5 Papua New Guinea earthquake. *Eng Geol* 297, 106504. <https://doi.org/10.1016/j.enggeo.2021.106504>
- Tanyaş, H., van Westen, C.J., Allstadt, K.E., Anna Nowicki Jessee, M., Görüm, T., Jibson, R.W., Godt, J.W., Sato, H.P., Schmitt, R.G., Marc, O., Hovius, N., 2017. Presentation and Analysis of a Worldwide Database of

Earthquake-Induced Landslide Inventories. *J Geophys Res Earth Surf* 122, 1991–2015. <https://doi.org/10.1002/2017JF004236>

Uemoto, J., Moriyama, T., Nadai, A., Kojima, S., Umehara, T., 2019. Landslide detection based on height and amplitude differences using pre- and post-event airborne X-band SAR data. *Natural Hazards* 95, 485–503. <https://doi.org/10.1007/s11069-018-3492-8>

Van Den Eeckhaut, M., Hervás, J., Montanarella, L., 2013. Landslide Databases in Europe: Analysis and Recommendations for Interoperability and Harmonisation, in: *Landslide Science and Practice*. Springer Berlin Heidelberg, Berlin, Heidelberg, pp. 35–42. https://doi.org/10.1007/978-3-642-31325-7_4

Vollrath, A., Mullissa, A., Reiche, J., 2020. Angular-Based Radiometric Slope Correction for Sentinel-1 on Google Earth Engine. *Remote Sens (Basel)* 12, 1867. <https://doi.org/10.3390/rs12111867>

Wang, F., Fan, X., Yunus, A.P., Subramanian, S.S., Alonso-Rodriguez, A., Dai, L., Xu, Q., Huang, R., 2019. Coseismic landslides triggered by the 2018 Hokkaido, Japan (Mw 6.6), earthquake: spatial distribution, controlling factors, and possible failure mechanism. *Landslides* 16. <https://doi.org/10.1007/s10346-019-01187-7>

Williams, J.G., Rosser, N.J., Kinsey, M.E., Benjamin, J., Oven, K.J., Densmore, A.L., Milledge, D.G., Robinson, T.R., Jordan, C.A., Dijkstra, T.A., 2018. Satellite-based emergency mapping using optical imagery: experience and reflections from the 2015 Nepal earthquakes. *Natural Hazards and Earth System Sciences* 18, 185–205. <https://doi.org/10.5194/nhess-18-185-2018>

Wilson, A.M., Jetz, W., 2016. Remotely Sensed High-Resolution Global Cloud Dynamics for Predicting Ecosystem and Biodiversity Distributions. *PLoS Biol* 14. <https://doi.org/10.1371/journal.pbio.1002415>

Xu, Y., Ouyang, C., Xu, Q., Wang, D., Zhao, B., Luo, Y., 2024. CAS Landslide Dataset: A Large-Scale and Multisensor Dataset for Deep Learning-Based Landslide Detection. *Sci Data* 11, 12. <https://doi.org/10.1038/s41597-023-02847-z>

Yang, Y., Rogers, B.M., Fiske, G., Watts, J., Potter, S., Windholz, T., Mullen, A., Nitze, I., Natali, S.M., 2023. Mapping retrogressive thaw slumps using deep neural networks. *Remote Sens Environ* 288, 113495. <https://doi.org/10.1016/j.rse.2023.113495>

Zhang, Z., Wang, H., Xu, F., Jin, Y.-Q., 2017. Complex-Valued Convolutional Neural Network and Its Application in Polarimetric SAR Image Classification. *IEEE Transactions on Geoscience and Remote Sensing* 55, 7177–7188. <https://doi.org/10.1109/TGRS.2017.2743222>

APPENDIX

Sentinel-1 SAR-based Globally Distributed Landslide Detection by Deep Neural Networks

Lorenzo Nava^a, Alessandro Mondini^b, Kushanav Bhuyan^a, Chengyong Fang^c, Oriol Monserrat^d, Alessandro Novellino^e and Filippo Catani^a

^a Machine Intelligence and Slope Stability Laboratory, Department of Geosciences, University of Padova, Padova, Italy

^b National Research Council, Research Institute for Applied Mathematics and Information Technologies, Genova, Italy;

^c State Key Laboratory of Geohazard Prevention and Geoenvironment Protection, University of Technology, 610059, Chengdu, China;

^d Department of Remote Sensing, Geomatics Research Unit, Centre Tecnologic de Telecomunicacions de Catalunya (CTTC), 08860 Barcelona, Spain;

^e British Geological Survey, Nicker Hill, Keyworth, Nottingham, NG12 5GG, UK;

* Correspondence: lorenzo.nava@phd.unipd.it;

Copernicus Global Land Cover Layers (CGLS-LC100) Collection 3

The Copernicus Global Land Cover Layers (CGLS-LC100) Collection 3 (https://developers.google.com/earth-engine/datasets/catalog/COPERNICUS_Landcover_100m_Proba-V-C3_Global#dois) provides a comprehensive land cover classification system with 23 main discrete classes. This classification is aligned with the UN Food and Agriculture Organization's (FAO) Land Cover Classification System (<https://www.fao.org/documents/card/en/c/c41f08a4-e612-45d8-b569-b751f27a3542/>).

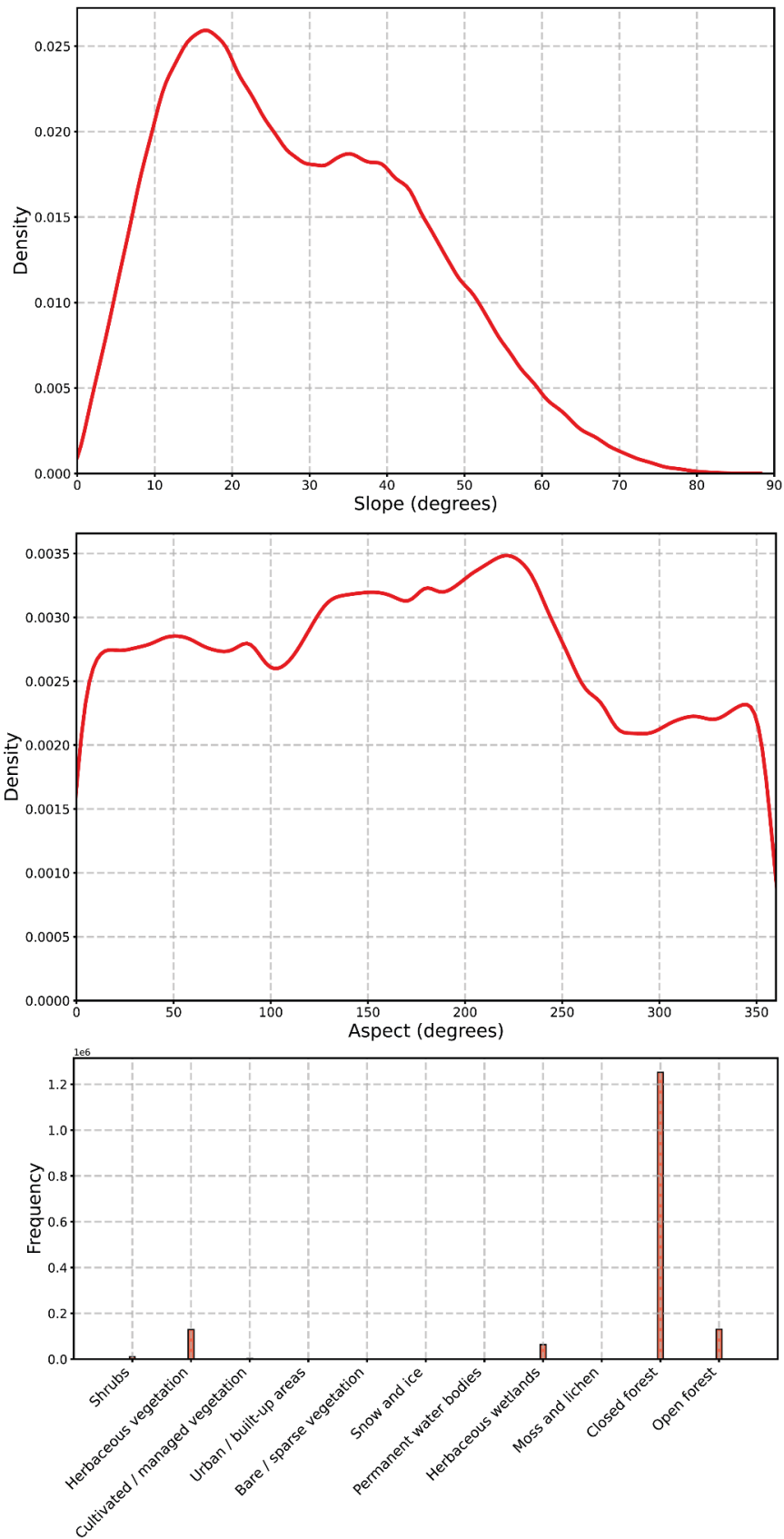


Figure A1: Distribution of slope, aspect, and landcover in the landslide scars used for the descending orbit datasets in the training dataset for the 60_12 temporal stack combination in the six study areas used to perform the comparison between the VV and VV_VH combinations.

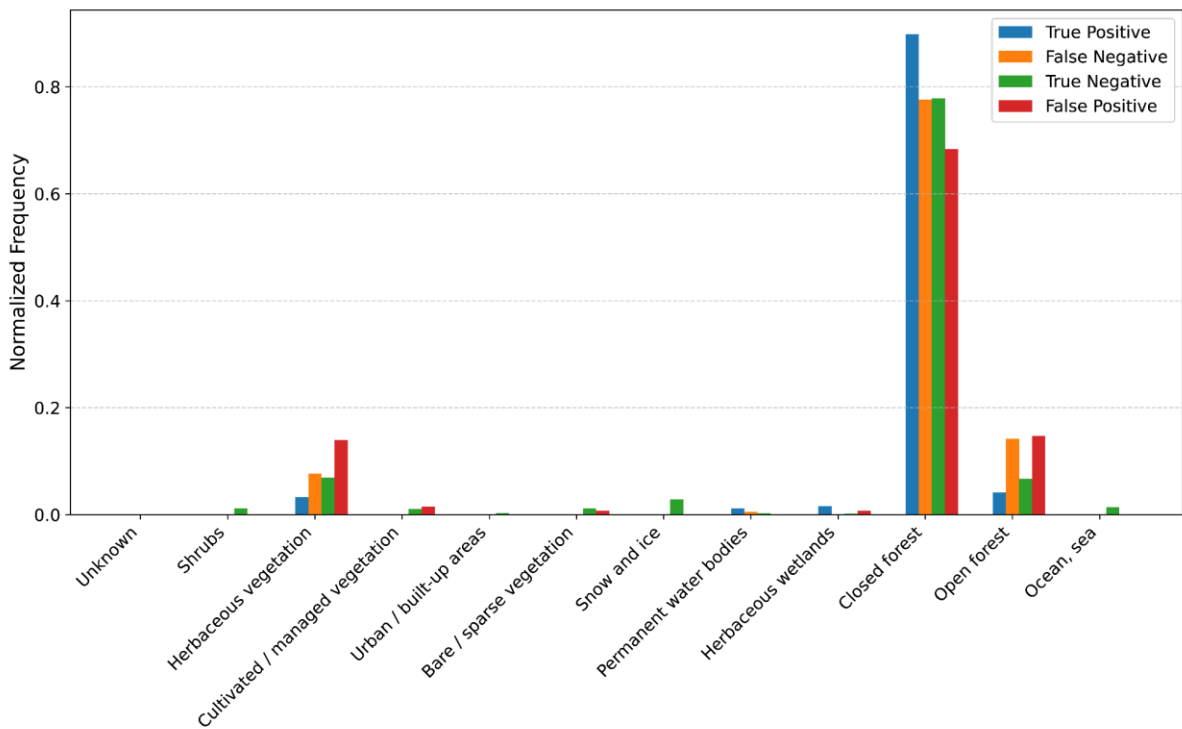


Figure A2: Distribution of majority class of landcover in the test dataset for the classification results of the 60_12 temporal stack combination in the six study areas used to perform the comparison between the VV and VV_VH combinations.

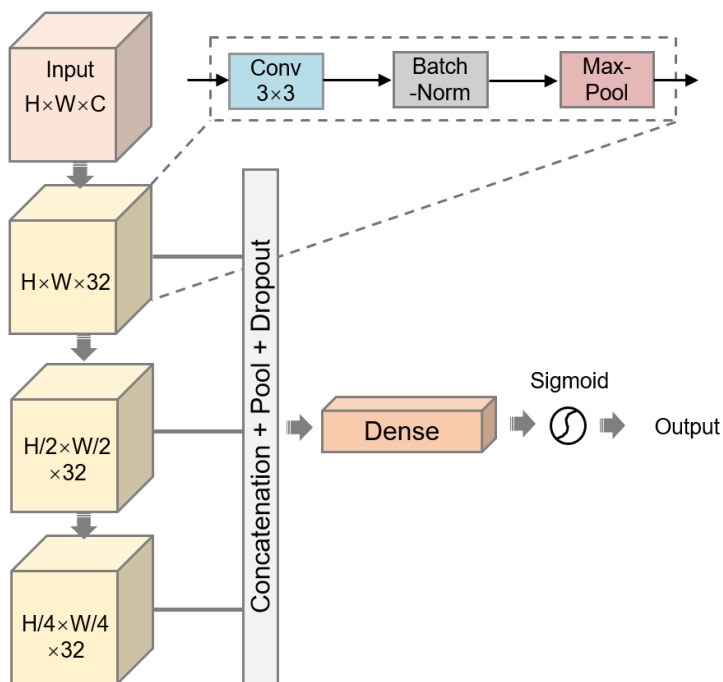


Figure A3: CNN model architecture used.